Flow-Induced Vibration of an Underwater Lazy Wave Cable in Unidirectional Current

R. Moideen^a, V. Venugopal^{a*}, J.R. Chaplin^b and A.G.L. Borthwick^a

^aSchool of Engineering, The University of Edinburgh, UK

Abstract

This paper describes measurements of the flow-induced vibration of an instrumented model cable in a lazy wave configuration immersed in unidirectional currents in the 2 m deep FloWave Facility at the University of Edinburgh. The cable model, designed to represent a dynamic power cable used in offshore renewable energy structures for electricity transmission, has an external diameter (D) of 31 mm and a mass ratio of 1.22. The current speed was varied from 0.1 to 0.9 m/s and its direction was set at 0, 90, and 180 degrees relative to the initial longitudinal axis of the cable. An underwater Qualisys motion capture system measured the in-line (IL) and cross-flow (CF) displacement components at 36 locations along the length of the submerged cable. Local displacements, response frequencies, and travelling wave modes are determined for reduced velocity $U_r \in (5.29, 47.69)$, and Reynolds number Re $\in (10^3, 10^3)$ 10⁴). It is found that the root mean square (RMS) values of the displacement components exhibited an increasing trend with reduced velocity reaching 0.40D in the in-line direction and 0.45D in the cross-flow direction. For reduced velocity in the range from 5.29 to 10.58, the cable exhibited single frequency vibrations. For $U_r > 10.58$, the cable experienced broad-banded, multi-frequency responses. Along the cable, certain locations were found to execute distinct circular, elliptical, nearly linear, and figure-ofeight orbits at low U_r . A sudden phase shift was observed along the cable length, related to unsteady vortex-induced vibration (VIV), which effectively prevented lock-in occurring at high U_r .

Keywords: Dynamic power cable, Vortex-induced vibration, Lazy wave, Hydro-elastic cable, Unidirectional current, Reduced velocity

Highlights:

- Cable RMS displacement components increase progressively with reduced velocity.
- Cross-flow displacement is larger than in-line displacement at the same frequency.
- At higher Re, cable vibration shifts from mono- to multi-frequency response.
- Local cable displacement trajectories include non-stationary chaotic oscillations.

^bFaculty of Engineering and the Environment, University of Southampton, UK

^{*}Corresponding author, at University of Edinburgh Email address: v.venugopal@ed.ac.uk

1. Introduction

Marine power cables play a crucial role in transmitting electricity from ocean-based renewable energy devices to onshore power grids. Such cables are particularly susceptible to fatigue damage due to dynamic loading from ocean currents, waves and vessel motions. Of particular concern is vortex-induced vibration (VIV), which can promote cable failure. VIV is caused by alternating vortex shedding in the near wake of a cable, which leads to transverse and in-line vibrations relative to the flow direction. It is well known that VIV becomes amplified when lock-in occurs as the cable natural frequency synchronises with the vortex shedding frequency, leading to increased drag and reducing the fatigue life of the cable. Hydrodynamically, VIV due to currents stands out as a leading cause of marine power cable failure, as distinct from installation errors(Rentschler et al., 2019). An understanding of VIV is therefore an essential prerequisite in the design and maintenance of marine cables.

Extensive investigations (see e.g., Vandiver, 1993; Blevins, 1990; Vandiver, 1993; Sarpkaya, 2004; Williamson & Govardhan, 2004, 2008) have revealed that certain non-dimensional parameters, including the Reynolds number, Strouhal number, aspect ratio, damping ratio, mass ratio, amplitude ratio, frequency ratio, and force coefficients, are key to the vortex-induced vibration dynamics of long, flexible cylinders. At lock-in, complicated vibrational patterns can occur along the length of a slender hydro-elastic cylinder. Historically, research into the flow-induced dynamics of slender cables has focused on top-tensioned members in uniform and sheared currents (see e.g., Chaplin et al., 2005; Govardhan & Williamson, 2006; Huera Huarte et al., 2006; Huera-Huarte & Bearman, 2009; Sarpkaya, 2004). Many studies have examined the VIV of flexibly mounted rigid vertical, inclined, straight and curved cylinders when the flow direction was perpendicular to the longitudinal axis of the cylinder (Jain & Modarres-Sadeghi, 2013; Lie & Kaasen, 2006; Vandiver et al., 2009; Xu et al., 2018). Morooka & Tsukada (2013) conducted physical model tests on a catenary marine riser that rested on the bed and was connected to a fixed support at the top. Due to laboratory constraints, the cable diameter was 8 mm and the resulting Reynolds number of 500-600 was far below the site value of 10⁵. Fan et al. (2015) recorded bending strains at six locations on a catenary flexible cylinder riser of diameter 20 mm. In both studies, the risers were positioned concave to the incoming current. Chaplin & King (2018) explored the behaviour of a nontensioned catenary riser configured in both convex and concave orientations relative to an incoming steady current; the riser comprised a low-bending-stiffness cylinder of diameter 56 mm and length 5.6 m, achieving Reynolds number up to 7x10⁵.

Consistent scaling of power cables is a major challenge in physical modelling. Govardhan & Williamson (2006) observed that, within the subcritical regime, larger amplitude responses occurred at higher Reynolds numbers, often reaching values twice those predicted by modified Griffin plots, despite the presence of high damping. This dependence on Reynolds number has prompted further research on the forces acting on marine power cables at high Reynolds numbers, especially for cables with

a lazy wave configuration. Raghavan & Bernitsas (2011) investigated the dependence of VIV on Reynolds number, spanning laminar to turbulent flow regimes (10⁴ < Re < 10⁶), using rigid circular cylinders with elastic supports. Their analysis revealed substantial differences in VIV behaviour occurred between low and high Reynolds numbers, with peak amplitude responses observed at high Reynolds numbers. In a study of long flexible risers in uniform and sheared currents, Resvanis et al. (2012) found the amplitude of vibration and the lift coefficient were sensitive to Reynolds number, and that the Strouhal number reduced with increasing Reynolds number.

It has proved difficult to achieve high Reynolds number flows in scaled physical experiments involving cables, given that both global and local dynamics require careful consideration. Nevertheless, to obtain reliable data by which to validate theoretical models, it is important to ensure that the scaled model tests effectively represent dynamic behaviour. Numerous studies (Franzini et al., 2016; Morooka & Tsukada, 2013; Pereira et al., 2013; Pesce et al., 2017; Trim et al., 2005) have highlighted the difficulties encountered in setting the correct diameter and aspect ratio in physical model tests, especially when a relatively large diameter is necessary to reach high Reynolds numbers. Unconventional approaches have therefore been used to achieve both dynamic and geometric similarity in experimental setups, as discussed by Chaplin et al. (2005). Rateiro et al. (2016) carried out a detailed review of the dynamic characteristics and non-dimensional parameters required to scale catenary riser models. They used a silicone tube filled with stainless steel microspheres to achieve dynamic similarity with a cylinder of largest outside diameter. While matching the exact properties of a full-scale model is often impractical due to facility limitations, it remains vital that the global geometry and bending responses are accurately represented in marine power cable tests at high Reynolds numbers.

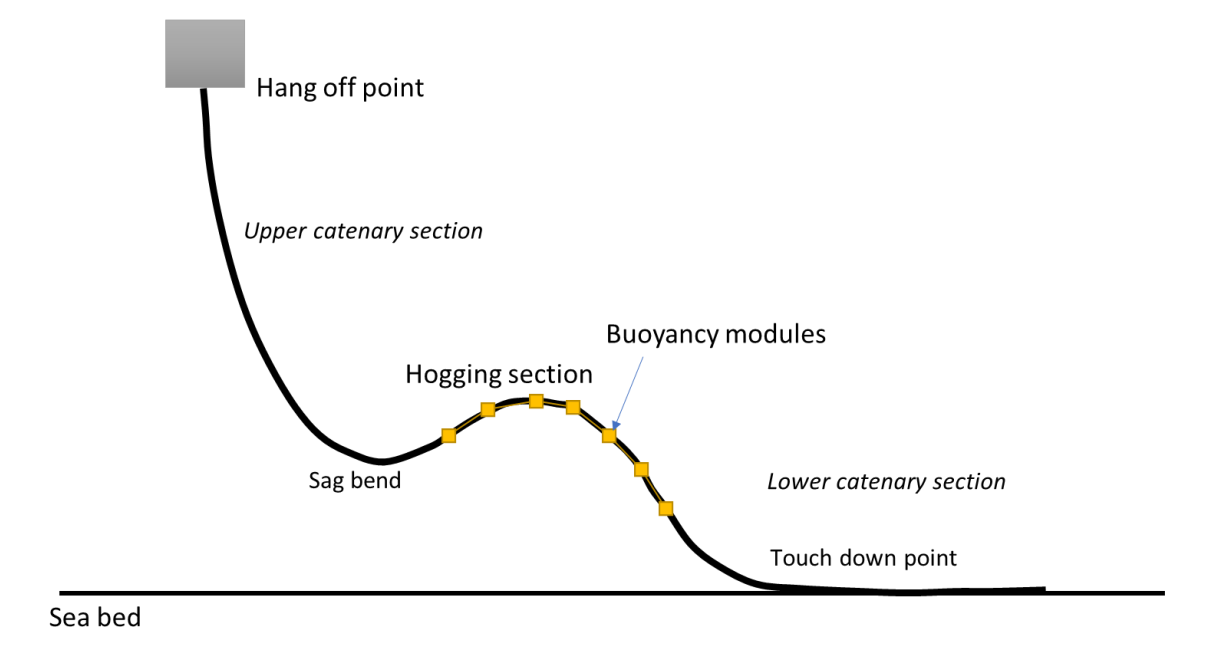


Figure 1: Schematic representation of a Lazy wave power cable configuration

In offshore practice, there is growing preference for the lazy wave configuration of marine cables (see Figure 1) given its superior performance compared against the catenary configuration regarding maximum tension and fatigue failure. The lazy wave configuration has further benefits owing to its ease of installation, lower buoyancy requirements, and reduced need for subsea hardware, making it a cost-effective and streamlined option (Martinelli et al., 2010). The integration of buoyancy modules serves to decouple platform motions from the touchdown point, thereby reducing the risk of failure in the touchdown zone.

The vortex-induced vibration (VIV) response of a cable with a lazy wave profile differs significantly from that of its straight and catenary counterparts. Important factors that alter the dynamic response are the geometric nonlinearity introduced by the curved surface of the cylinder and the presence of larger diameter buoyancy modules in the buoyancy section. For example, Assi et al. (2014) and Zhu & Lin (2018) identified higher response amplitudes for rigid cylinders in a concave configuration compared to a convex one, with sustained responses occurring beyond the usual synchronization region. Similarly, Chaplin & King (2018) observed distinct vortex shedding patterns and forces in catenary profiles based on the concave or convex curvature of the cable. The structural flexibility of the buoyancy section allows the cable to respond dynamically to fluid forces, introducing multiple vibration modes with varying curvature, resulting in complicated fluid-structure interactions (Srinil et al., 2009). For highly inclined cables, the amplitude of displacement oscillations increases, and the lock-in region, the maximum oscillation amplitude, and normalized reduced velocity all deviate from the corresponding normal-incidence cases (Jain & Modarres-Sadeghi, 2013). Moreover, interference effects from hydrodynamic coupling cause vibrations in one section of the cable to influence vibration responses elsewhere along the cable, similar to the wake-induced vibrations of tandem cylinders (Assi et al., 2006, 2009, 2014). For VIV, while vibration amplitudes tend to decrease at higher reduced velocity, the wakeinduced vibrations display an opposite trend, with their amplitude increasing as the reduced velocity decreases. In fact, the difference in behaviour between convex and concave configurations is partly due to such wake interference.

The lower bending stiffness of marine power cables, compared to risers, means that they have quite different natural frequencies and lock-in phenomena which are particularly sensitive to the mass ratio. Cheng et al. (2016) and Yin (2022) conducted experimental studies on steel lazy wave configuration risers, focusing on VIV response characteristics and associated displacements. In comparing their measured data against numerical predictions by OrcaFlex, Chang et al. and Yin reported some discrepancies due to varying hydrodynamic coefficients. More recently, experimental investigations byJara-Bravo et al. (2024) on cylinders with buoyancy modules yielded intriguing results, highlighting differences in drag, added mass, and lift coefficients compared to those observed in infinite cylinder scenarios. Despite numerous numerical studies estimating VIV for lazy wave cable configurations (Rentschler et al., 2019; Thies et al., 2012; Zhao et al., 2021), experimental validation remains vitally important, especially as attention shifts from marine risers towards dynamic power

cables. Unlike steel risers used in offshore oil installations(Quéau et al., 2013; Zhu et al., 2020), marine power cables possess unique characteristics such as the absence of internal fluid, lower bending stiffness, and increased flexibility – all of which require targeted research. To the authors' knowledge, no extensive experimental results have previously been presented in the literature for lazy wave marine power cables, particularly at higher Reynolds numbers.

In this study, we present an experimental investigation into the dynamic behaviour of a marine power cable in lazy wave configuration under varying current conditions. We employ a distorted scale model with an increased cable diameter to maintain the Reynolds number (Re) in the range of 10³ to 10⁴, ensuring realistic dynamic behaviour akin to the sea. This work provides new insight into the response of the cable to different current speeds and directions (0°, 90°, and 180° relative to the longitudinal orientation of the initial lazy wave cable). Measured displacements in three dimensions, in-line and cross-flow amplitude responses, frequency responses, and cable displacement trajectories, are analysed and discussed in detail in the following sections. We believe that this study contributes to a deeper understanding of the dynamic behaviour of a marine lazy wave cable.

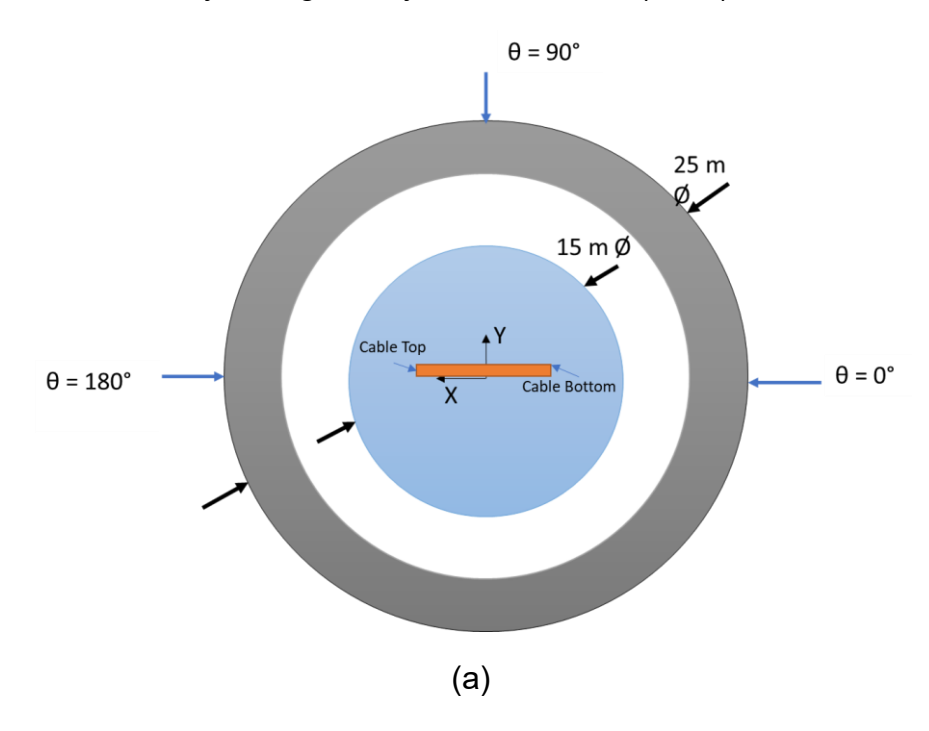
2. Experimental Setup - FloWave

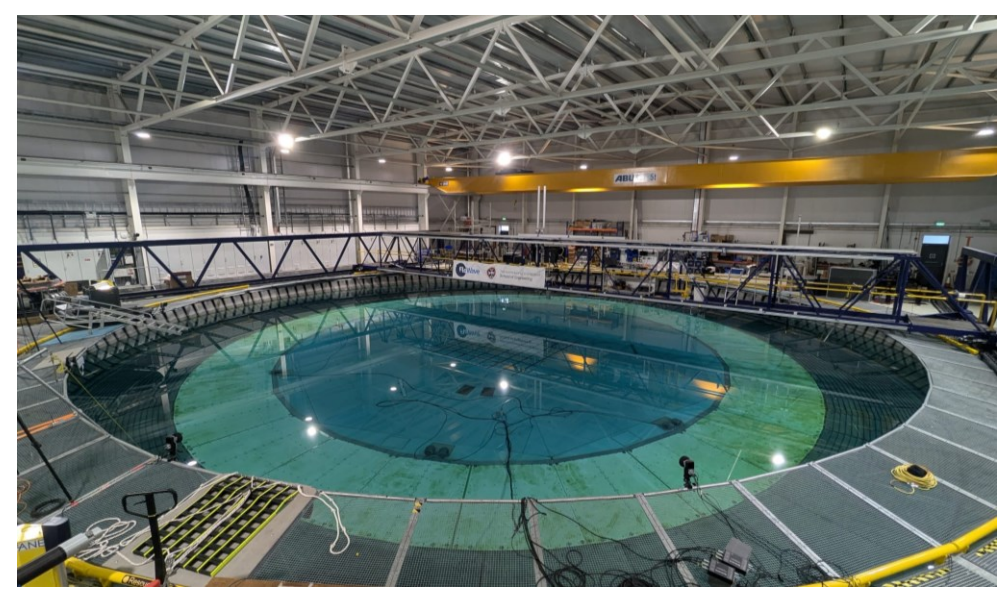
The physical tests were conducted at the FloWave Ocean Energy Research Facility (https://www.flowavett.co.uk/) in the University of Edinburgh. FloWave comprises a circular basin of 25 m diameter and 2 m water depth, and is capable of generating a unidirectional current. The currents are produced by 28 flow-drive units controlling 1.7 m impellers that independently drive flow anywhere at speeds of up to 1.6 m/s in any direction from 0 to 360°. For ease of model installation, the 15 m diameter central section of the tank floor can be raised above still water level. Figure 2 presents a plan view of the FloWave testing tank, showing the cable (from above) and the current directions considered herein.

2.1 Cable Model Setup and Instrumentation

To achieve a relatively high Reynolds number, low mass ratio, and low bending stiffness, the model cable had an outer diameter of 31 mm and was of length 5 m. It is important to note that part of the cable was inserted into the top and bottom connections at the FloWave tank, which reduces the effective length to 4.93 m. Table 1 lists the dimensions and material properties of the constituent elements of the cable construction. The cable had an inner flexible dummy core fabricated from a 3-core H07RN-F power cable of diameter 9.8 mm (see Figure 3(a)). A total of 28 IP68-rated strain gauges, sourced from Techni Measure Ltd (Doncaster UK), were connected in full bridge configurations at seven strategic locations (4 strain gauges affixed at each location) along the core cable at 0.5 m intervals. The strain gauge wires were threaded through four-chambered spacers (see Figure 3(b)-(d)). These spacers, measuring 20 mm in length and 24 mm in diameter, were spaced at 20 mm intervals along the length of the cable. The core, strain gauges, and spacers were then sealed in a silicone tube

of 25 mm inner diameter and 31 mm outer diameter. The spacers, crafted from 3D printed material (Polylactic acid), were then securely bonded to the outer platinum-cured silicone tube, preventing any relative movement. The final model consisted of a 5 m long smooth-walled flexible cable Figure 3(e), with steel tubes at both ends to ensure proper fixation to the tank floor and the top of the load cell. Its interior was filled with water to eliminate kinks in the wall and ensure the cable functioned as a single entity. Note that the strain measurement analysis will not be reported in this paper; instead, part of the analysis is given by Moideen et al. (2024).





(b)

Figure 2: FloWave test facility: (a) schematic plan view showing cable model (not to scale) and (b) an image of FloWave basin.

Table 1: Cable model dimensions and material properties

Scale model					
Length (m)	5 m (effective length is 4.93 m)				
The total mass of cable	5.157 kg (excluding end				
	connections is 4.526 kg)				
Outside diameter (m)	0.031				
Inner core cable	H07RN-F 3-core rubber cable				
Inner core cable diameter (m)	9.8 mm				
Inner core cable mass per unit length	134 g/m				
(g/m)					
Mass ratio of cable	1.22				
Submerged length of cable in water	4.16 m				
Touchdown zone	1.35 m				
Buoyancy section	1.12 m				
Top section	2.279 m				
Buoyancy modules					
Outside diameter	70 mm				
Inside diameter	31 mm				
Length	40 mm				
Density	100 kg/m ³				
No. of modules	5				
3D printed bobbins					
Number of bobbins	118				
Mass (g/piece)	4.4				
Total mass	519.2 g				
Silicon tube mass per m	250 g/m				
Mass of strain gauges wires	461 g				
Mass of water filled + dummy wires	1108.2 g				

To achieve the lazy wave configuration, buoyancy modules were used to elevate the hogging section. The modules were manufactured from Divinycell PVC foam material of density 100 kg/m³ (see Figure 4). Table 1 lists their dimensions. The top of the cable extended above the water surface (0.77 m above SWL) and was connected to a six-component load cell, which was secured to the main gantry in FloWave (see Figure 5(a)). The bottom end of the cable was anchored to the tank floor. The load cell measured the force and moment components of the cable; note that these measurements are not presented herein for brevity. Upon lowering the tank floor to its operating level, the cable then formed a lazy wave configuration (Figure 5 (b)). The bending stiffness of the cable was evaluated by means of a structural bending test. Table 2 presents the structural properties, including the natural frequency and damping ratio obtained from a free decay test. Further details of the free decay test in air may be found in Moideen et al. (2025). A scaling factor of 1:50 was adopted for

the study, except for the cable diameter. All other structural parameters and input current conditions adhere to Froude scaling. The experiments were conducted at 1:50 scale, with current speeds varying from 0.1 to 0.9 m/s, corresponding to full-scale current speeds of 0.707 to 6.36 m/s. This range is consistent with real-world tidal currents observed at sites of the European Marine Energy Test Centre (https://www.emec.org.uk/) in the Orkney and Pentland Firth regions in Scotland, where typical values range from approximately 1 m/s in general coastal regions to 3.5–4.5 m/s in high-current areas.

Table 2: Measured and estimated cable properties.

Property	Value	
Bending stiffness, <i>EI</i> (Nm²)	0.217 Nm ²	
Natural frequency in air, $f_n(Hz)$	0.61 Hz	
Damping in air	0.0048	

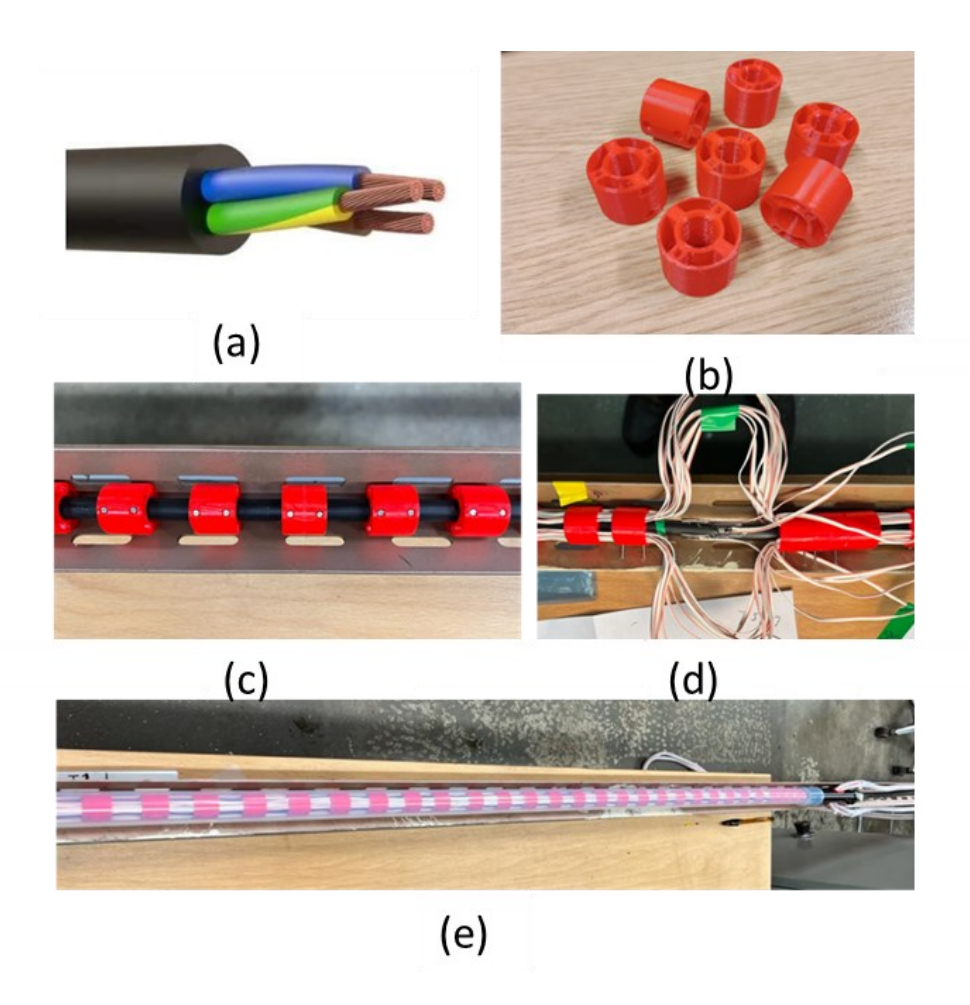


Figure 3: Model cable: (a) inner core dummy cable; (b) 3D printed spacers; (c) inner cable inserted through spacers and secured; (d) strain gauges affixed to the inner core cable with integrated strain gauge wires, and (e) cable model encased in a platinum-cured silicone tube.

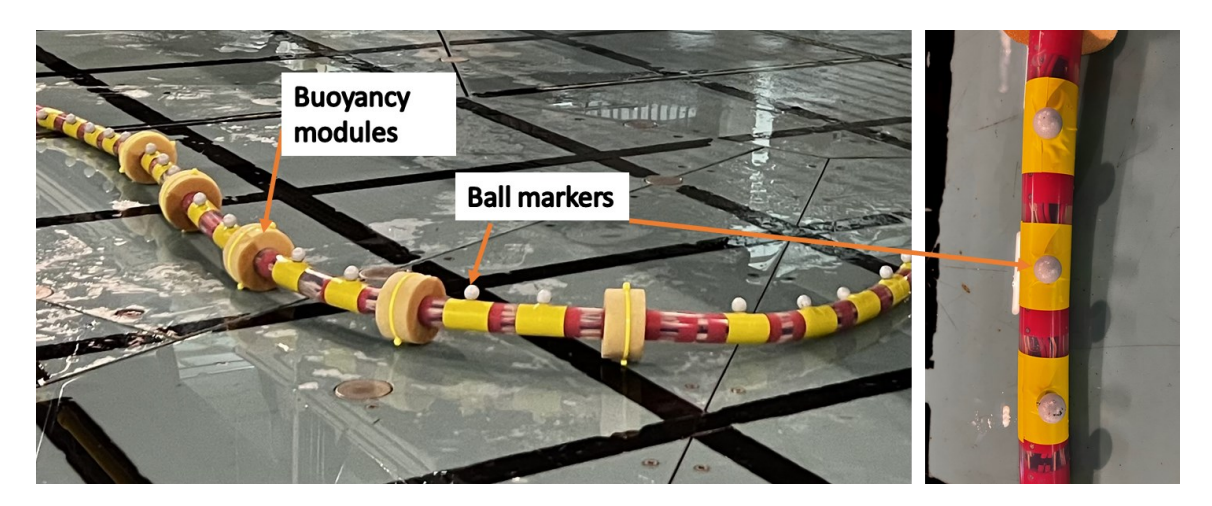


Figure 4: Cable with buoyancy modules and ball markers attached.

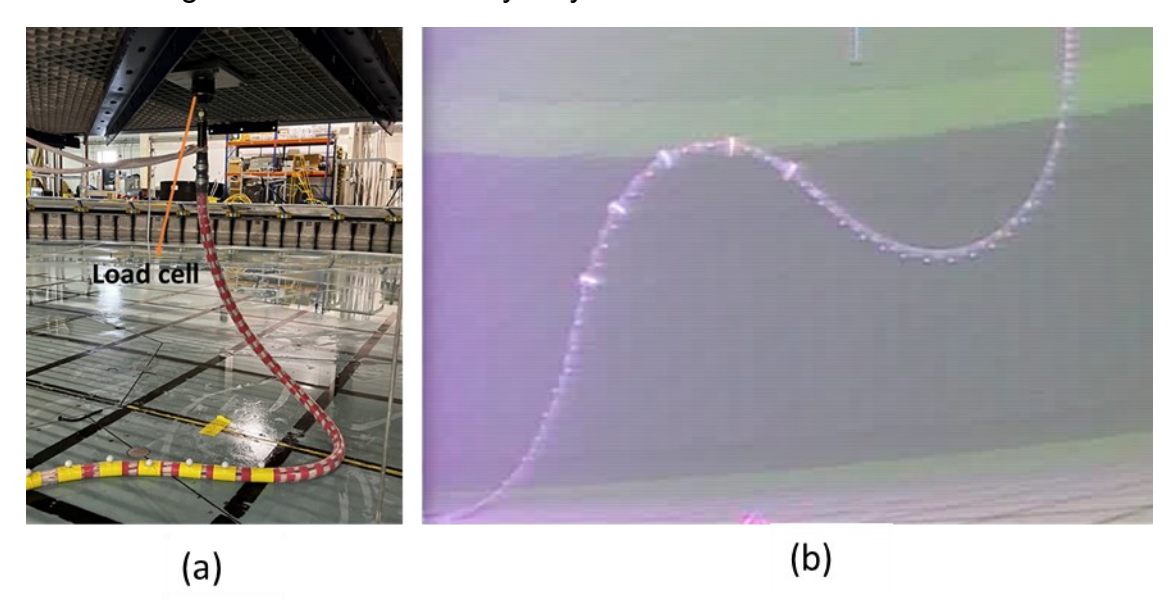


Figure 5: (a) Photograph of model cable with one end fixed at the top to the load cell on the tank gantry and the other end fixed onto the tank floor; and (b) cable profile captured by the underwater camera.

To estimate the natural frequency and damping characteristics in air, the cable, configured in a catenary profile with buoyancy modules and fixed at both ends, was subjected to free decay tests in the FloWave facility. The tests yielded a natural frequency in air of 0.61 Hz. The cable was then submerged in water to achieve the lazy wave profile, and free decay tests were conducted in different directions. The measured natural frequency in water for the lazy wave configuration ranged from 0.125 Hz (in-plane) to 0.141 Hz (out-of-plane). However, the free decay response in water exhibited very strong damping to the detriment of further analysis.

Numerical simulations also were performed using OrcaFlex (https://www.orcina.com/) based on the measured structural properties of the cable model. Given the relatively low mass of the cable (i.e., 0.919 kg/m), the simulation results proved to be highly sensitive to parameter variations. For comparison purposes, OrcaFlex simulations of

additional free decay tests were conducted in a catenary configuration (without buoyancy modules as including buoyancy elements will alter the shape from catenary) in water, yielding a natural frequency in water of 0.451 Hz.

Using the measured value of natural frequency in air and assuming an added mass coefficient of 1.0, we estimated the natural frequency in water of the cable in catenary configuration from Equation (1)

$$f_{Nw} = f_{Na} [1 + (\pi C_a / 4\mu)]^{-0.5}$$
 (1)

where, f_{Nw} is the natural frequency of the cable in water, where f_{Na} is the natural frequency of the cable in air, C_a is the added mass coefficient, and μ is the mass ratio (Vandiver, 1993).

Table 3 lists the modal frequencies obtained by OrcaFlex for both the in-plane and out-of-plane directions. The results indicate that the natural frequencies in the lazy wave configuration are significantly lower than those in the catenary configuration. This reduction is attributed to the absence of tension in the lazy wave setup and its geometric arrangement.

Table 3: Modal frequencies (f_m) catenary vs Lazy wave

Mode number	Catenary Profile	Lazy wave profile	Plane		
1	0.23	0.09	Y-plane		
2	0.45	0.13	X plane		
3	0.47	0.19	Y-plane		
4	0.64	0.27	X plane		
5	0.73	0.30	Y-plane		
6	0.97	0.40	X plane		
7	1.01	0.52	Y-plane		
8	1.07	0.64	X plane		
9	1.32	0.73	Y-plane		
10	1.41	0.91	X plane		
11	1.66	0.99	Y-plane		
12	1.67	1.22	X plane		
13	2.02	1.29	Y-plane		
14	2.04	1.58	X plane		
15	2.39	1.64	Y-plane		

Using Table 3, we selected the second-mode natural frequency ($f_{m(2)} = 0.127$ Hz) to normalize the in-plane response and the third-mode frequency ($f_{m(3)} = 0.1857$ Hz) to normalize the out-of-plane response. Figure 6 presents the corresponding mode shapes providing additional insight into the structural response of the cable under different configurations.

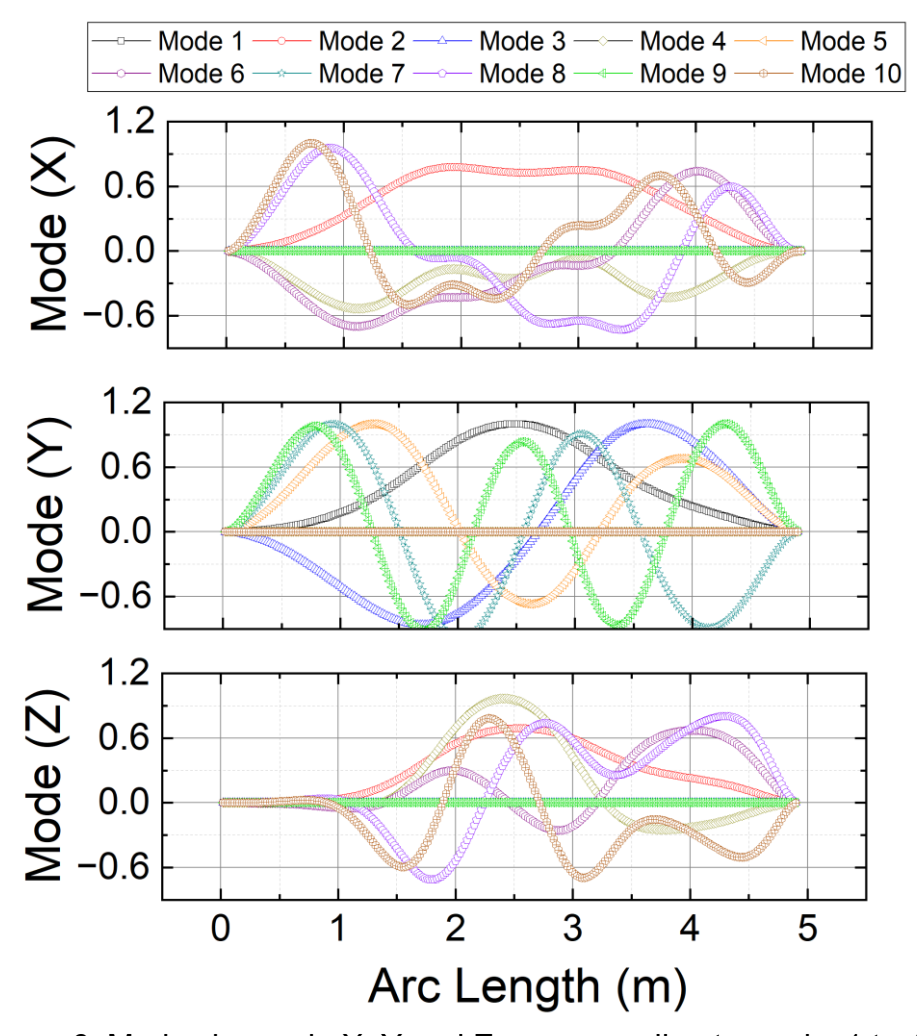


Figure 6: Mode shapes in X, Y and Z corresponding to modes1 to 10.

A Qualisys motion capturing system measured local cable displacements in global *X*, *Y*, *Z* coordinates. Six cameras tracked the motion of the cable, with a sampling frequency of 128 Hz. The camera positions were carefully selected to optimize the performance of the motion-capturing system in evaluating the movement of the flexible cable. Reflector ball markers (the white balls in Figure 4) of diameter 16 mm were placed at a further 37 locations to represent accurately the movement of the cable (see Figure 6). Marker 1 on the cable was positioned at a water depth of 1.5 m from the tank bottom, while Marker 37 was located 0.15 m from the cable's bottom end. It should be noted however that the method had a limitation in that the markers could alter the vortex shedding pattern; an aspect that merits further attention. In future work, we intend to replace the markers by thin reflector tapes wrapped around the cable to assess the impact of the markers. Despite these challenges, we believe the cable displacement measurement system provided valuable data, even when the current was of relatively high speed.

3. Results and Discussion

Figure 7 shows the displacement profile in the *X-Z* plane of the cable in still water. The black squares show the position of each marker. The red markers at the top and bottom show the cable's connection points. Figure 7 illustrates the configuration of the cable in the FloWave tank.

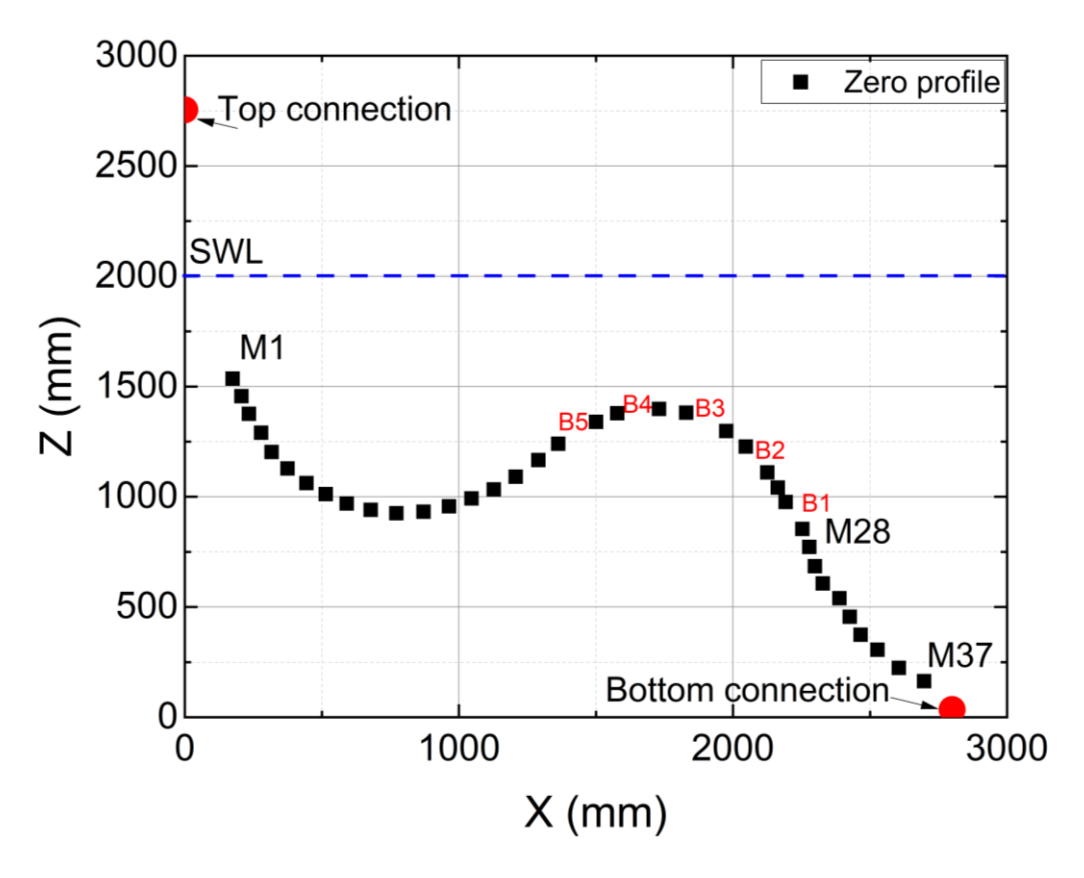


Figure 7: Lazy wave cable profile in still water with Qualisys markers (black squares).

3.1 Cable Displacement

Marker displacements were measured for the lazy wave cable in currents of speed 0.1, 0.2, 0.3, 0.4, 0.5, 0.6, 0.7 and 0.8 m/s, and direction 0, 90, and 180° relative to the longitudinal axis of the cable (Figure 8). At 0 and 180 degrees the current is parallel to the plane occupied by the cable when in still water. At 90 degrees it is normal to it (i.e., along the Y direction) as seen in Figure 8. Table 4 presents the current speed and the corresponding reduced velocity ($U_r = U/f_nD$), where f_n is the natural frequency of the cable and D is its outer diameter. For our analysis, we have chosen U_r based on f_n in air for subsequent presentations. All displacement results presented in this paper are normalized by the cable diameter, D = 31 mm. As shown in the previous table, the lower modal frequencies of the lazy wave profile are relatively small and exhibit minimal variation within a narrow range. Moreover, whereas the first mode of reduced velocity is commonly applied for rigid or straight members, this approach may

be misleading for a flexible cable where higher modes could drive the response frequency. Mode decomposition becomes particularly challenging as the flexible cable moves in three dimensions, and so we believe that use of the natural frequency in air as a constant provides a more pragmatic approach. However, the values obtained using f_m in water (Table 4) remain relevant for comparative analysis, as the added mass effect in water can influence the dynamic response.

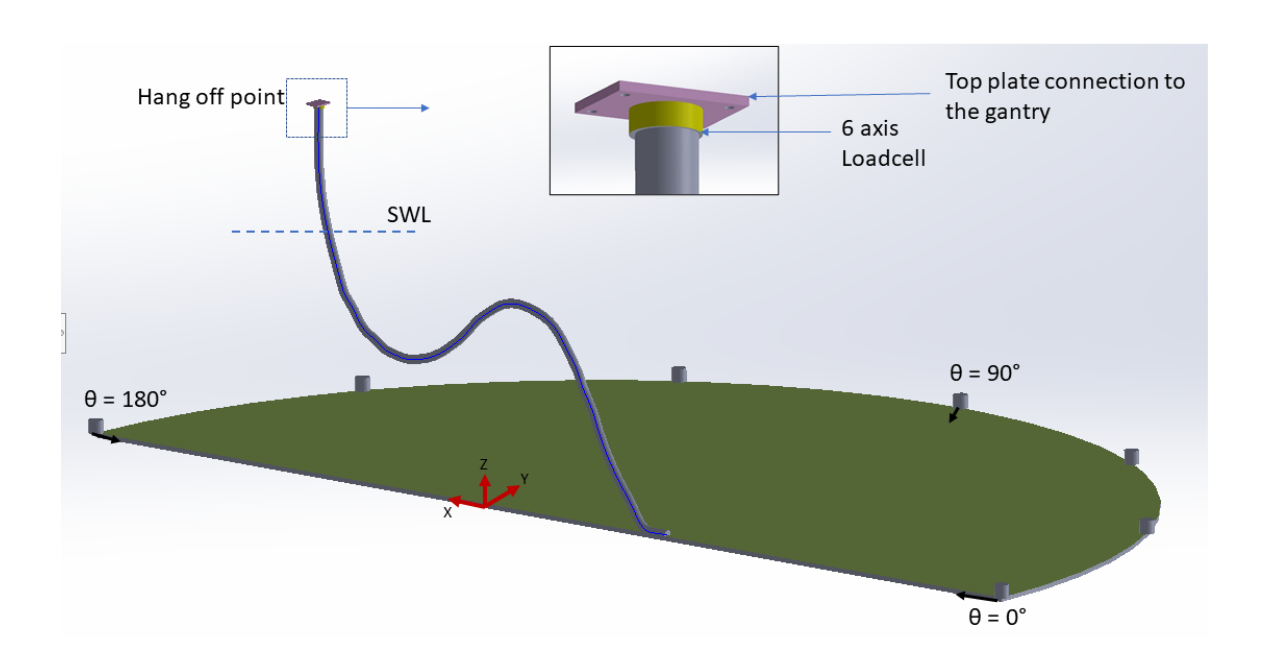


Figure 8: Schematic diagram showing Lazy wave configuration and directions of current in FloWave tank

Table 4: Current speed U and associated reduced velocity U_r

U (m/s)	0.1	0.2	0.3	0.4	0.5	0.6	0.7	0.8	0.9
$U_{\rm r}(f_n {\rm in air})$	5.28	10.57	15.86	21.15	26.44	31.7	37.01	42.30	47.59
U _r (f _m in water)	24.81	49.63	74.44	99.26	124.07	148.88	173.70	198.51	223.35

The flexible cable in the lazy wave configuration underwent increasingly large amplitude motions between its fixed ends as the current speed was progressively increased. Figure 9 depicts the position of the displaced cable in the vertical X - Z and horizontal X - Y planes for different current speeds and directions, along with the original cable profile in still water.

For current direction $\theta = 0^{\circ}$, the cable alters its shape from a lazy wave (U = 0.1 to 0.4 m/s) to an inclined straight profile (U = 0.7 to 0.8 m/s) in the vertical X - Z plane as the current speed increases (Figure 9 (a)). The cable also undergoes transverse movement that is roughly linear but of smaller amplitude in the horizontal X - Y plane

(Figure 9 (b)). An offset in the Y-direction of 10-15 cm is observed in the zero profile in Figure 9(b) and is attributed to the weight imbalance caused by the buoyancy modules and the inherent self-twisting of the cable assembly when installed in the FloWave tank. As a result, the cable was not perfectly normal to the current at all locations. For currents of direction $\theta = 90^{\circ}$, the cable again straightens out in the vertical plane but with a much more pronounced gradient (see results for U = 0.7 and U = 0.8 m/s in Figure 9 (c)). In the horizontal plane, the cable increasingly bows outwards in the Y-direction as the current speed is increased (Figure 9 (d)). For U =0.7 and U = 0.8 m/s, the amplitude of the horizontal deflection in the X – Y plane for θ = 90° far exceeds that for θ = 0°. For θ = 180°, the cable is pushed in the streamwise direction (Figure 9 (e)) compared to the θ = 90° results; here the cable appears to be very steeply, even vertically, inclined as it touches the bed, and shifted a short distance horizontally (Figure 9 (f)). Thus, for all the current speeds considered, the cable is oriented at varying angles to the incident flow rather than being uniformly normal to the current at all locations. This is in contrast to a straight member subjected to a uniform flow perpendicular to its axis, where vortex shedding and hydrodynamic loading follow a well-defined pattern. In the case of the flexible lazy wave configuration, the varying orientation along the span results in spatially non-uniform hydrodynamic forces, influencing the vortex-induced vibration (VIV) response differently across different segments of the cable.

The cable profiles in Figure 9 display the movement of the cable, which has been filtered to isolate the vibration component. To examine local displacements of the cable, we have removed low-frequency components below 0.2 Hz, which is likely emanate from low frequency oscillations of the current. The filtered signal helps us visualize the flow-induced vibrations, and so the filter was applied to all displacement data considered from here on. The displacement time histories presented in Figure 10 are normalized with respect to the cable outside diameter.

Figure 10 (a, b, & c) presents the normalized raw displacement time history obtained using the Qualisys system at marker location M30 in the X, Y, and Z directions (X/D, Y/D, and Z/D) for current speed of 0.1 m/s and current directions $\theta = 0^{\circ}$, 90° , and 180° . To analyse the motion relative to the current direction, the displacement components in the X, Y, and Z directions were transformed into in-line and cross-flow displacements using direction cosines, as detailed in Appendix A. The results indicate that the in-line displacement is very small for current directions of 0° and 180° , but significantly higher in the X-direction when the current is at 90° . This is consistent with expected behaviour given that the cable exhibits greater response in the direction perpendicular to the incident flow. Figure 10 (a, b, & c) shows the IL (x_{IL}/D) and CF (y_{CF}/D) displacement components obtained after applying the transformation equations from Appendix A. A distinct beating behaviour is observed in the time histories presented in Figure 10, particularly evident for the current direction $\theta = 90^{\circ}$, with the strongest manifestation at the bottom marker location, M30. This behaviour, characterised by a modulated amplitude envelope arising from closely spaced

frequency components, reflects the interaction of multiple structural vibration modes. However, it is not shown here, as the response propagates upward along the cable, similar beating patterns are observed at all marker location with the amplitude diminishes progressively from bottom to top.

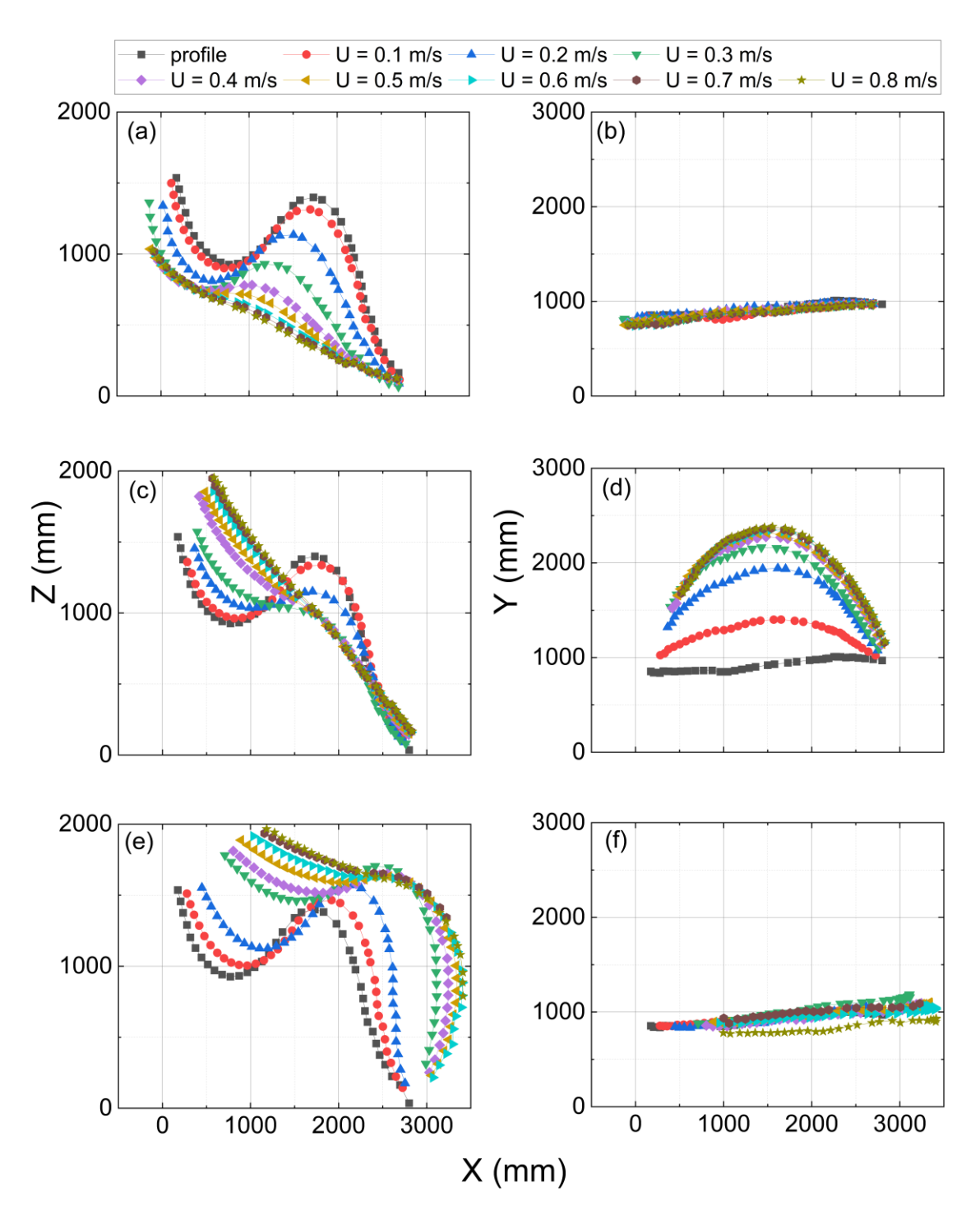


Figure 9: Lazy wave cable profiles in unidirectional current of speeds from 0.1 to 0.8 m/s: (a) vertical X–Z plane, θ = 0°; (b) horizontal X–Y plane, θ = 0°; (c) vertical X–Z plane, θ = 90°; (d) horizontal X–Y plane, θ = 90°; (e) vertical X–Z plane, θ = 180°; and (f) horizontal X–Y plane, θ = 180°.

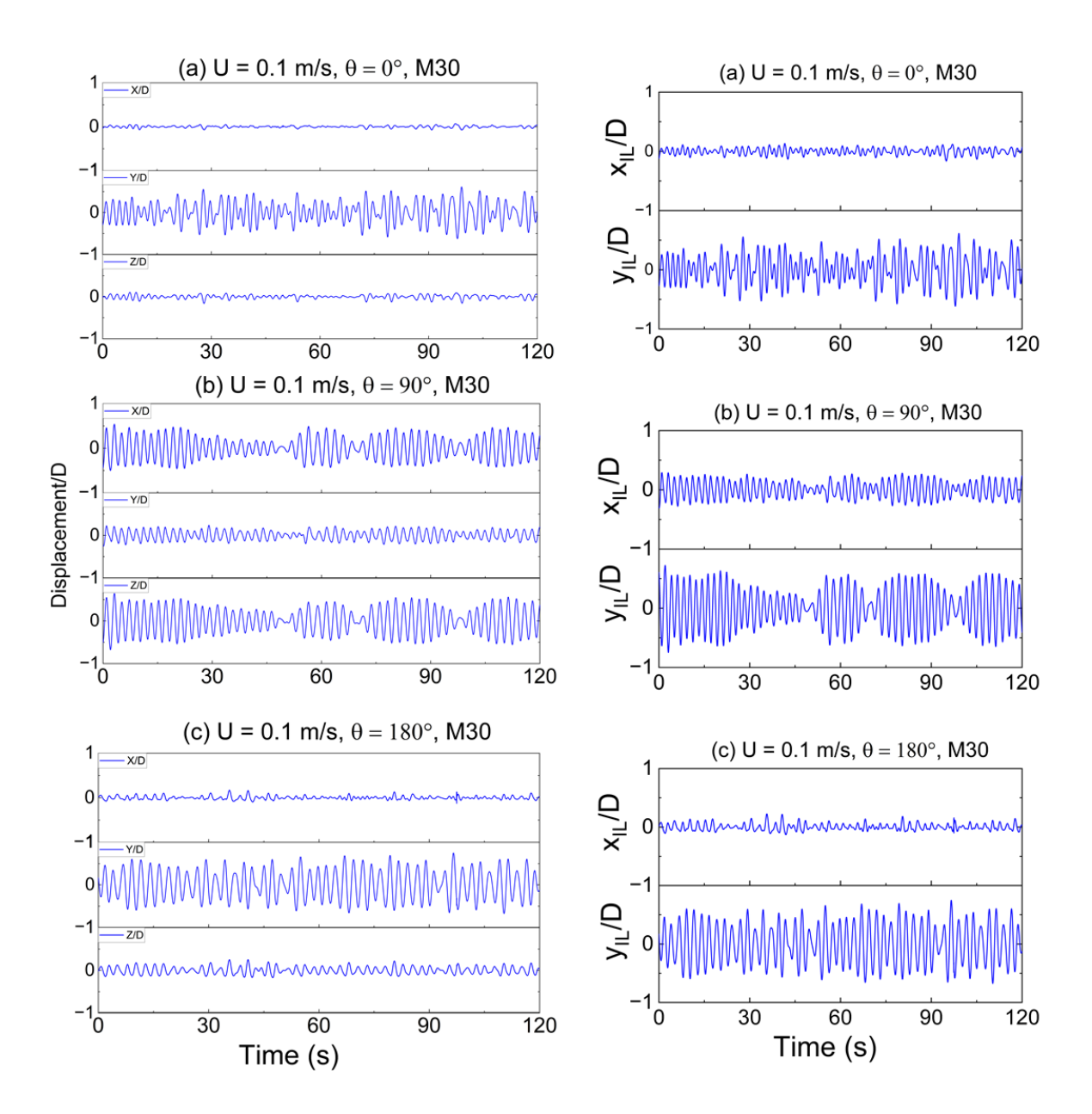


Figure 10: Normalised displacement time histories (X/D, Y/D and Z/D) at marker location M30 for current speed of 0.1 m/s. For original measured signals; (a) $\theta = 0^{\circ}$; (b) $\theta = 90^{\circ}$; (c) $\theta = 180^{\circ}$ and converted signals to In-line and cross-flow directions; (d) $\theta = 0^{\circ}$; (e) $\theta = 90^{\circ}$; and $\theta = 180^{\circ}$.

In the Figure 11, the left column depicts the normalized cross-flow displacement (y_{CF}/D) time history, and the right column depicts the same displacement time history for 10 seconds to identify the fluctuations with increasing current speed. For brevity, we consider the in-line and cross-flow displacements at a single marker location of M21. Subplots (a) to (g) correspond to increasing current speed from 0.1 to 0.7 m/s. For a current speed of 0.1 m/s (Figure 11 (a)), the cross-flow displacement time histories are relatively smooth and exhibit low amplitude fluctuations. As the current speed increases to 0.2 m/s (Figure 11 (b)), there is a slight increase in the amplitude compared to U = 0.1 m/s, but the regularity seen in the cross-flow direction for U = 0.1

m/s starts to disappear. For U = 0.3 m/s (Figure 11 (c)), the displacement amplitudes have increased significantly. The motion is more irregular and contains higher frequency components. This trend continues with U = 0.4 m/s (Figure 11 (d)), where the amplitude and irregularity of oscillations increase markedly, indicating stronger interactions between the current and the cable. The displacement patterns transition from smooth and periodic (U = 0.1 m/s) to highly irregular at higher current velocities (U = 0.5 to 0.7 m/s). The displacements appear chaotic for U = 0.5 to 0.7 m/s, indicating strong and complex interactions between the current and the cable dynamics.

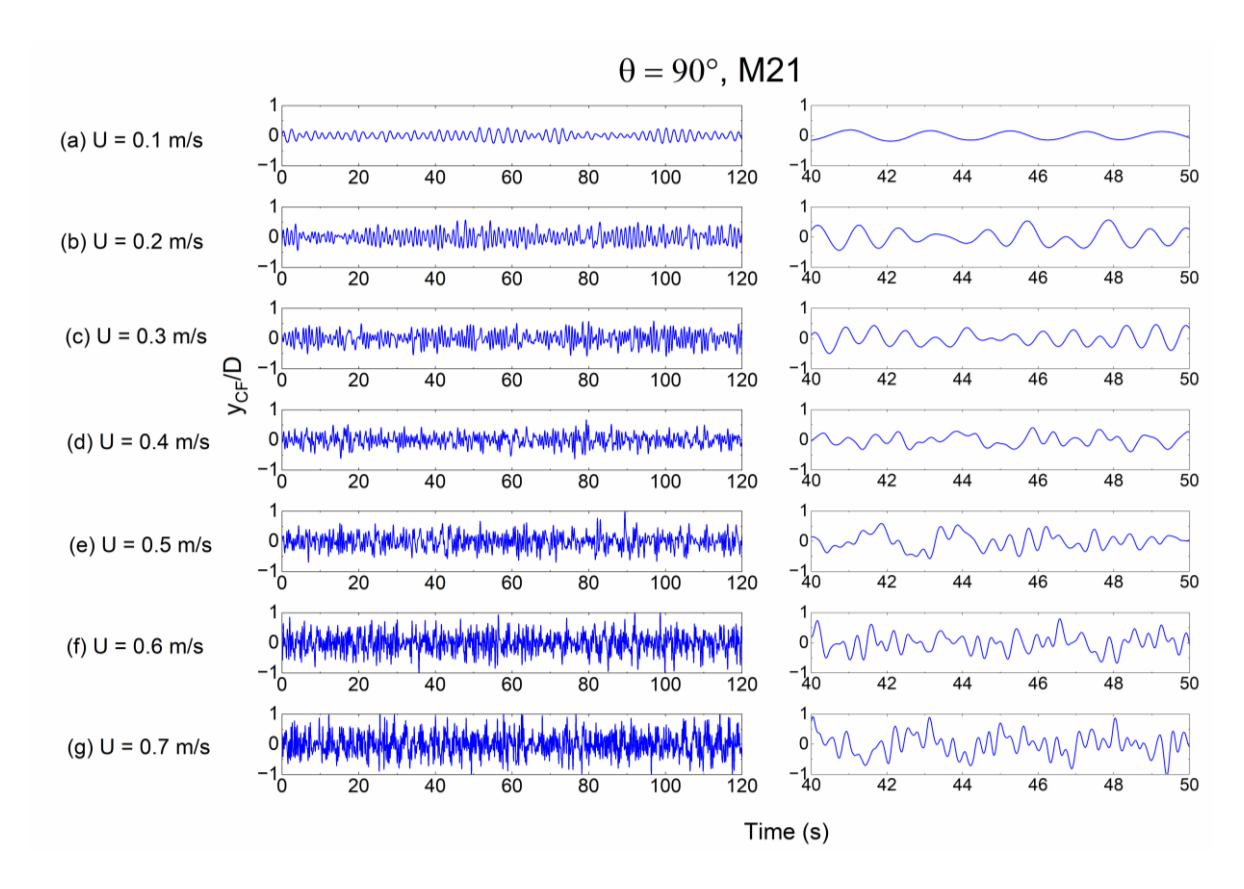


Figure 11: Time histories of normalised in-line cross-flow displacements of the cable at marker location M21 for varying current speed: (a) U = 0.1 m/s (b) U = 0.2 m/s (c) U = 0.3 m/s, (d) U = 0.4 m/s, (e) U = 0.5 m/s, (f) U = 0.6 m/s, and (g) U = 0.7 m/s. (right hand side shows the crossflow displacement for 10 seconds)

Further to analyse the effect of marker location, Figure 12 shows the variation of normalized in-line and cross-flow displacement components at selected marker locations and for a current speed of 0.4 m/s acting in the longitudinal direction of the cable ($\theta = 0^{\circ}$). The in-line displacement component has higher magnitude in the midsection of the cable, from M14 to M19. Notably, marker M15 to M19 (Figure 12 (c)) exhibits a higher in-line displacement for the same current speed. M19 is situated at the start of the buoyancy section immediately after the first buoyancy module, where the cable diameter increases due to the presence of the buoyancy modules. Interestingly, the displacements reduce from M20 (Figure 12 (f)) towards the bottom

of the cable, where higher cross-flow displacements are observed. Overall, the vibration amplitude increases progressively as the current speed increases, with cross-flow displacements typically exceeding in-line displacements. However, this behaviour can vary depending on the marker location. For example, at marker M19, the in-line displacement occasionally exhibits larger magnitude. This can be attributed to the marker being located near a node of the excited cross-flow vibration mode, where cross-flow (CF) motion is suppressed. Additionally, the current is not uniformly normal to the cable along its entire length, resulting in spatially varying hydrodynamic forces. As the orientation of the cable relative to the current varies along the length of the cable, its displacement response exhibits spatial non-uniformity. Certain regions of the cable experience minimal motion due to local hydrodynamic shielding and structural stiffness, while others undergo significant displacement, influenced by flow-induced excitation and varying distribution of tension in the cable.

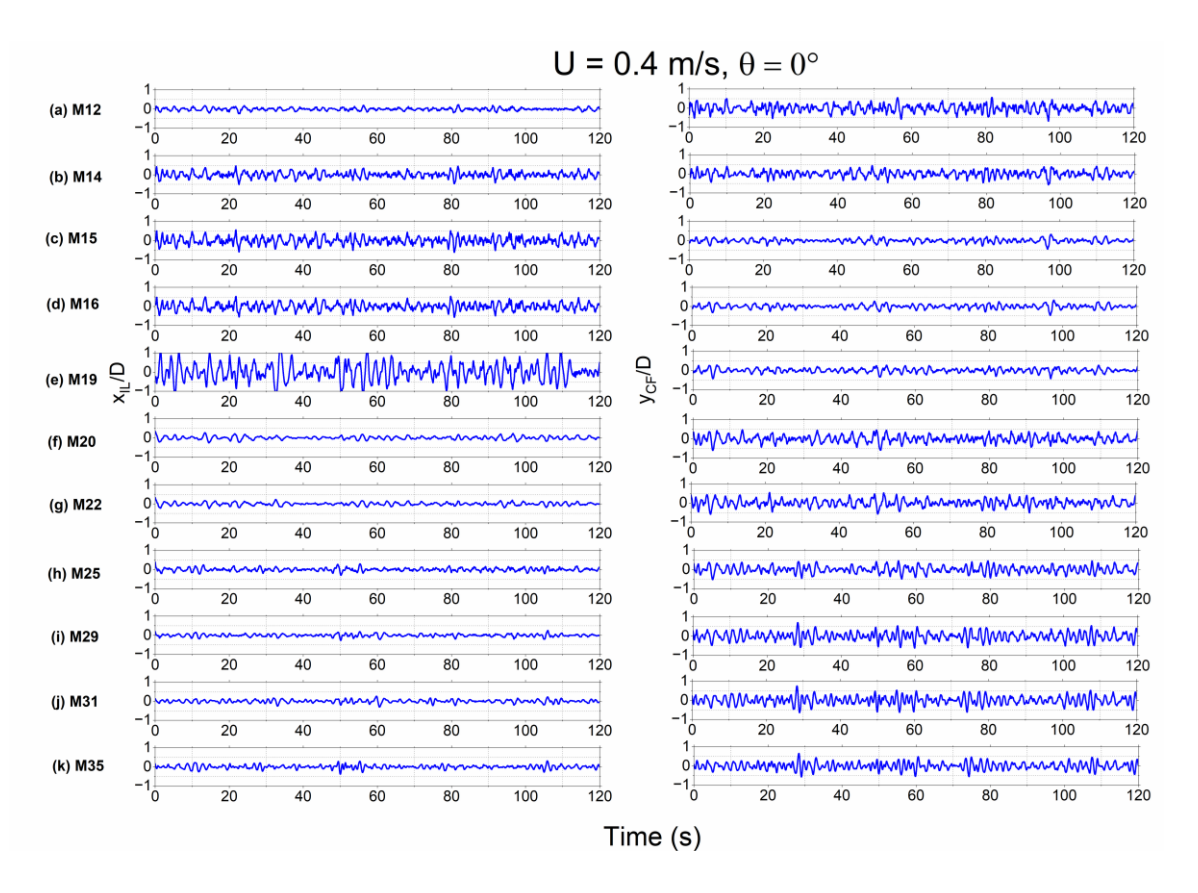


Figure 12: Time histories of normalised in-line and cross-flow displacements of the cable in a current of speed 0.4 m/s and direction 90° at markers: (a) M12, (b) M14, (c) M15, (d) M16, (e) M19, (f) M20 (g) M22 (h) M25 (i) M29 (j) M31 and (k) M35.

3.2 Cable Displacement Trajectories

Figures 13 illustrate a selection of typical trajectories obtained in-line and cross-flow displacements for current directions of 0°, 90°, and 180° at top, sag region, buoyancy section and bottom markers along the cable, under current speed of 0.1 m/s. Each trajectory covers a time interval of 40 to 50 s. The shape of the displacement

trajectories varies significantly depending on the marker location along the cable and the direction of the approaching current.

The displacement trajectories of the lazy wave cable, as shown in Figure 13, vary significantly depending on marker location and current direction. Unlike the repeatable figure-eight patterns observed in catenary cables (Morooka et al., 2013), these trajectories are highly non-stationary and chaotic, influenced by cable geometry, hydrodynamic forces, and local tension and buoyancy variations.

For a 0° current direction (inline flow), the top markers (M3, M10) display compact, near-vertical loops, indicating minimal excitation in the upper span. Moving downward, sag-region markers (M16, M25) develop elongated elliptical trajectories, suggesting increased inline (x_{IL}) and cross-flow (y_{CF}) motion due to greater flexibility. The bottom section markers (M30, M36) show even more pronounced elongation, likely driven by vortex-induced vibration (VIV) and buoyancy-induced restoring forces. When the current is perpendicular (90°) to the cable, cross-flow displacement dominates. The top markers (M3, M10) exhibit irregular, scattered trajectories, indicative of chaotic vortex shedding with weak coupling between inline and cross-flow motion. In contrast, the bottom section (M30, M36) displays an elongated trajectory, while the sag-region markers (M16, M25) form moderately elliptical but unstructured loops, highlighting the complex, non-repetitive nature of the response. For a 180° current direction (opposing inline flow), the displacement patterns become increasingly irregular. The top markers (M3, M10) show small, distorted loops, suggesting reduced flow separation effects. The sag-region markers (M16, M25) exhibit elliptical or distorted paths, likely influenced by unsteady vortex shedding and fluctuating cable tension. A distinct boomerang-like trajectory is observed for M30 and M36, indicating intermittent synchronization between inline and cross-flow oscillations. Overall, the inline displacement magnitude remains relatively low compared to the cross-flow displacement for 0° and 180° current directions. In contrast, for 90° current direction, both inline and cross-flow motions exhibit higher amplitudes, indicating a stronger coupling between the two displacement components, likely driven by vortex-induced forces and cable dynamics.

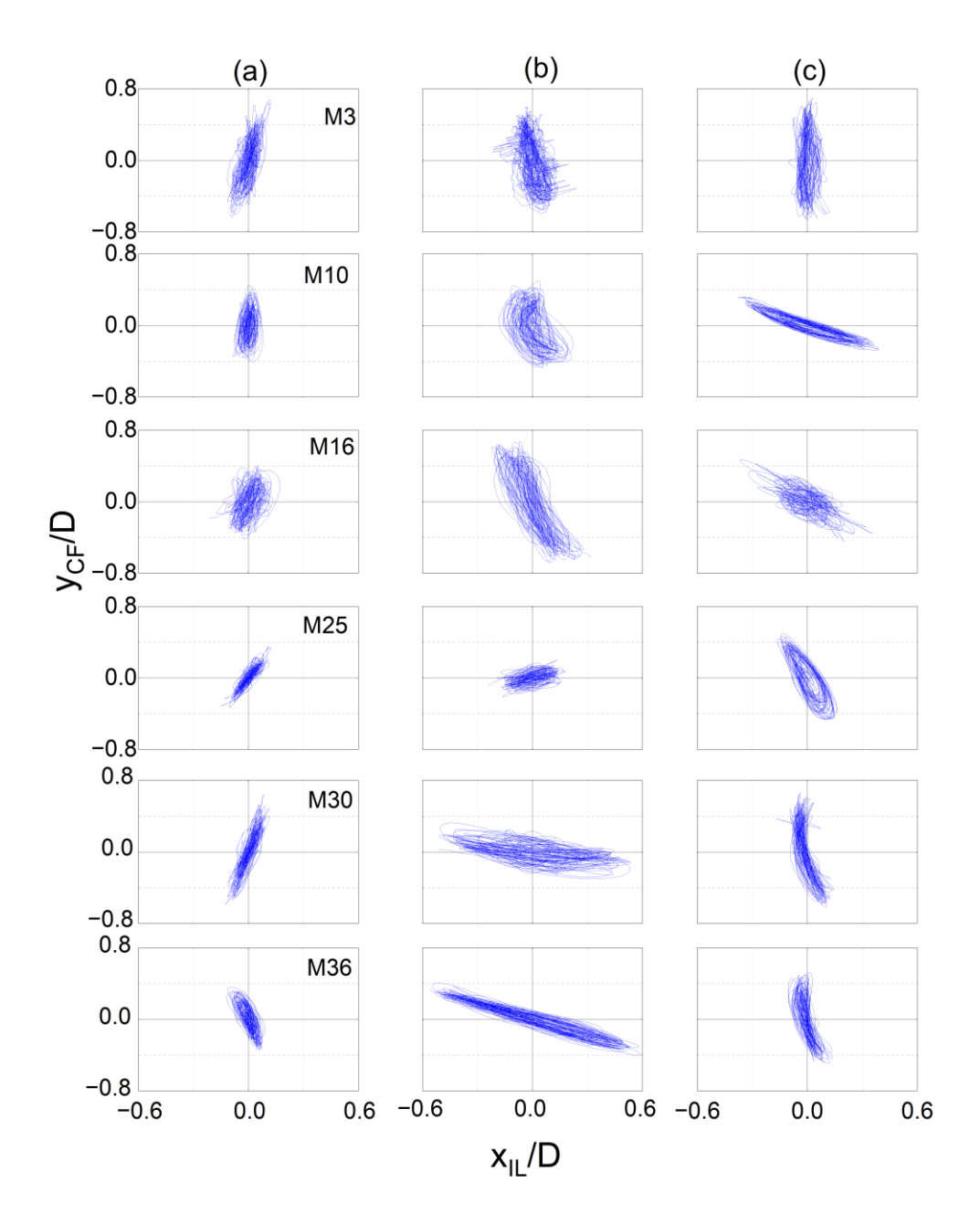


Figure 13: Trajectories drawn with the original signals for a current of 0.1 m/s acting in (a) 0°, (b) 90° and (c)180°.

Variational Mode Decomposition (VMD) is performed to separate the signal into intrinsic modes that represent the frequency components of each signal. VMD decomposes the signal into modes arranged in decreasing frequency order. Figure 14 (i) shows the inline and crossflow displacement time history (Figure 14(i): a) split into six intrinsic modes (figure 14 (i): b, c, d, e, & f), where the first few modes represent high-frequency components (figure 14 (i): b, c & d). The fifth and sixth modes exhibit frequencies of interest, identified as IM5 and IM6 (Figure 14(i): f & g). The trajectories of these modes (Figure 14(ii): f & g) are plotted along with their respective mode frequencies (Figure 14(iii): f & g), highlighting that the total component (Figure 14(a))

also contains periodic components (Figure 14(ii): f) and chaotic components (Figure 14(ii): g). Notably, the spectral frequencies of IM5 (Figure 14(iii): f) reveal that the inline frequency is about twice that of the cross-flow (CF) frequency. The original signal also shows an inline frequency component that is double the CF frequency, but with very low energy (Figure 14 (iii): a). This decomposition of signals provides clear insight into the frequency components present in the signal. It is also important to note that the magnitude of the inline displacement is very small. For the time history corresponding to a velocity of 0.1 m/s, the peak response frequencies in both inline and cross-flow directions are the same, corresponding to the 6th modal frequency of the structure. As the current magnitude increases, the signals become increasingly chaotic (Figure 14 (ii): g). The frequency variation at higher current speed will be discussed in the next section.

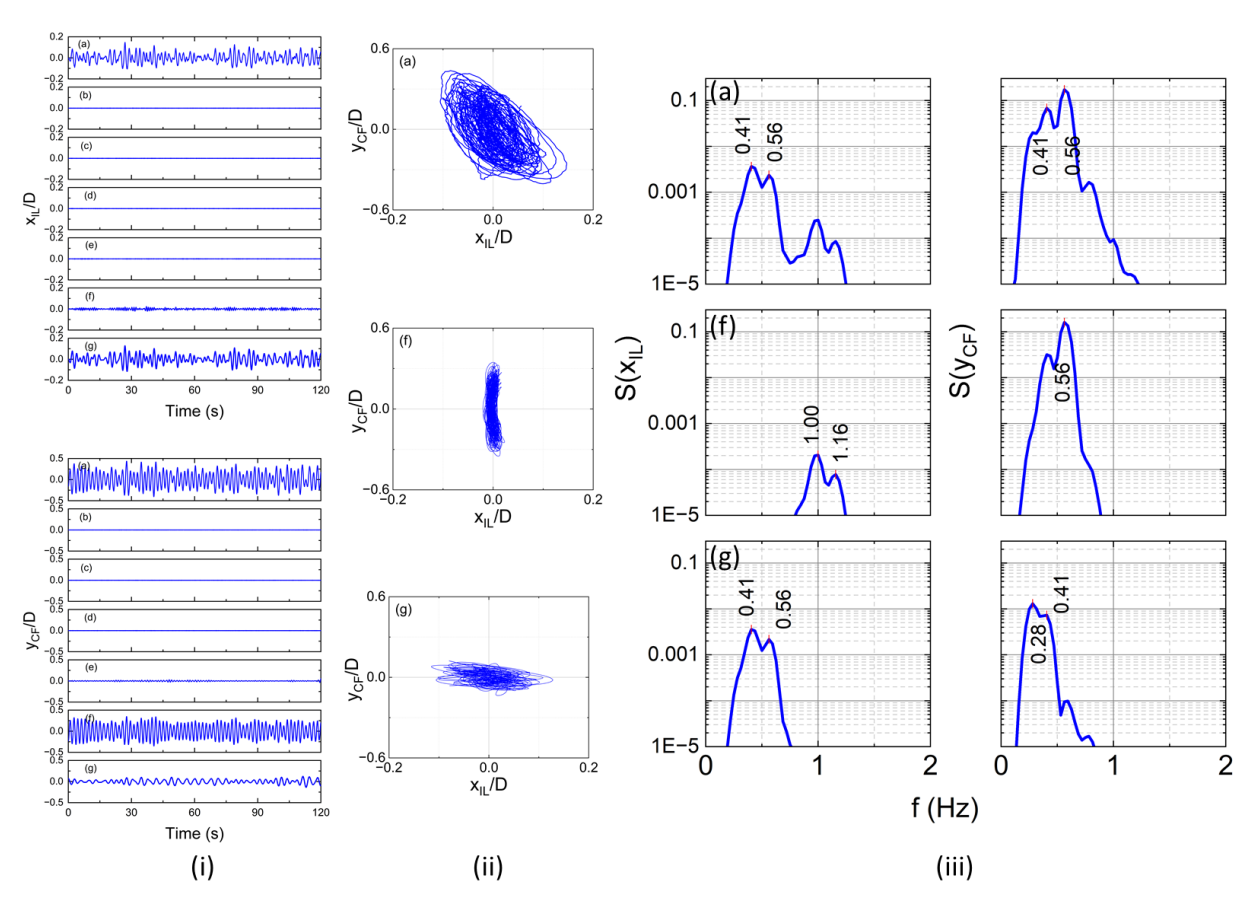


Figure 14: VMD of IL and CF displacement time histories: (i) left hand side - IMFs (b) to (g); (ii) middle - trajectories corresponding to original signal (a), IMF5 (f) and IMF6 (bottom); right hand side; (iii) spectral density plots for original signal (a), IMF5 (f) and IMF6 (g).

3.3 RMS displacements

We next examine the variations in root mean square (RMS) displacement, normalized by the cable diameter, at different locations along the cable. The largest RMS displacement typically occurs in the power-in region, where energy input from the flow is highest and displacements most pronounced. Figure 15 depicts the variation in normalized RMS displacements for current directions of 0°, 90°, and 180° as the current speed increases. When the flow direction is aligned with the cable longitudinal axis ($\theta = 0^{\circ}$), the normalized in-line displacement (x_{IL}/D) gradually increases with escalating current speed, as shown in Figure 15 (a). The normalised displacement is notably higher in the buoyancy section of the cable, due to its enlarged diameter which is not accounted for when normalizing displacements. At lower current speeds up to and including 0.4 m/s, the normalised cross-flow displacement (y_{CF}/D) is significantly larger, about 0.2D (Figure 15 (b)), compared to in-line displacements of approximately 0.12D (Figure 15 (a)). This suggests that the cross-flow vibrations prevail over in-line vibrations at lower current speeds when the flow direction is aligned with the cable. For $\theta = 90^{\circ}$, where the incident current is normal to the cable, the RMS displacements exhibit distinct patterns as shown in Figures 15 (c) & (d). As observed in Figure 15 (c), x_{IL}/D is generally higher at the top and bottom sections of the cable compared to the middle section. This indicates that regions of the cable furthest from the midsection are more susceptible to in-line motion when the cable orientation is perpendicular to the current direction. As the current speed increases, the in-line displacements become more pronounced near the ends of the cable, indicating a stronger response to the increased magnitudes of vortex shedding and associated drag force component acting along the length of the cable. Figure 15 (d) displays the normalised cross-flow displacement (y_{CF}/D) , which also peaks near the top of the cable. Notably, the normalized cross-flow displacements are significantly larger than the in-line displacements, with the y_{CF}/D values near the top and bottom of the cable being roughly twice those of x_{IL}/D observed for the same current direction. This indicates that the cable experiences stronger lateral forces, causing it to oscillate more vigorously in the cross-flow direction when the current is oriented perpendicular to the longitudinal axis of the cable. For θ = 180°, where the flow is aligned with the cable but in the opposite direction to $\theta = 0^{\circ}$, the RMS displacements have distinct characteristics, as depicted in Figures 15 (e) & (f). In Figure 15 (e), x_{\parallel}/D the displacement is more pronounced in the buoyancy section, as also observed for θ = 0°, and there is a noticeable shift in the displacement peaks along the length of the cable. This could be due to two mechanisms: the reverse flow direction altering the cable profile; and changes in the way vortices interact with the cable structure. Figure 15 (g) The cross-flow displacement (y_{CF}/D) is higher, particularly towards the ends of the cable. The displacement profiles suggest that the cable experiences different vortex shedding and wake interactions when the flow is reversed, leading to shifts in the points of maximum vibration. At a reduced velocity (U_r) of 5.28, there is a marked increase in CF displacement at specific points on the cable: at the bottom for $\theta = 0^{\circ}$ (Figure 15 (b)), at the middle for θ = 90° (Figure 15 (d)), and at both the top and bottom for θ = 180° (Figure 15 (g)). This suggests that U_r = 5.28 is a critical point regarding the vortex-induced vibrations (VIV) of the cable.

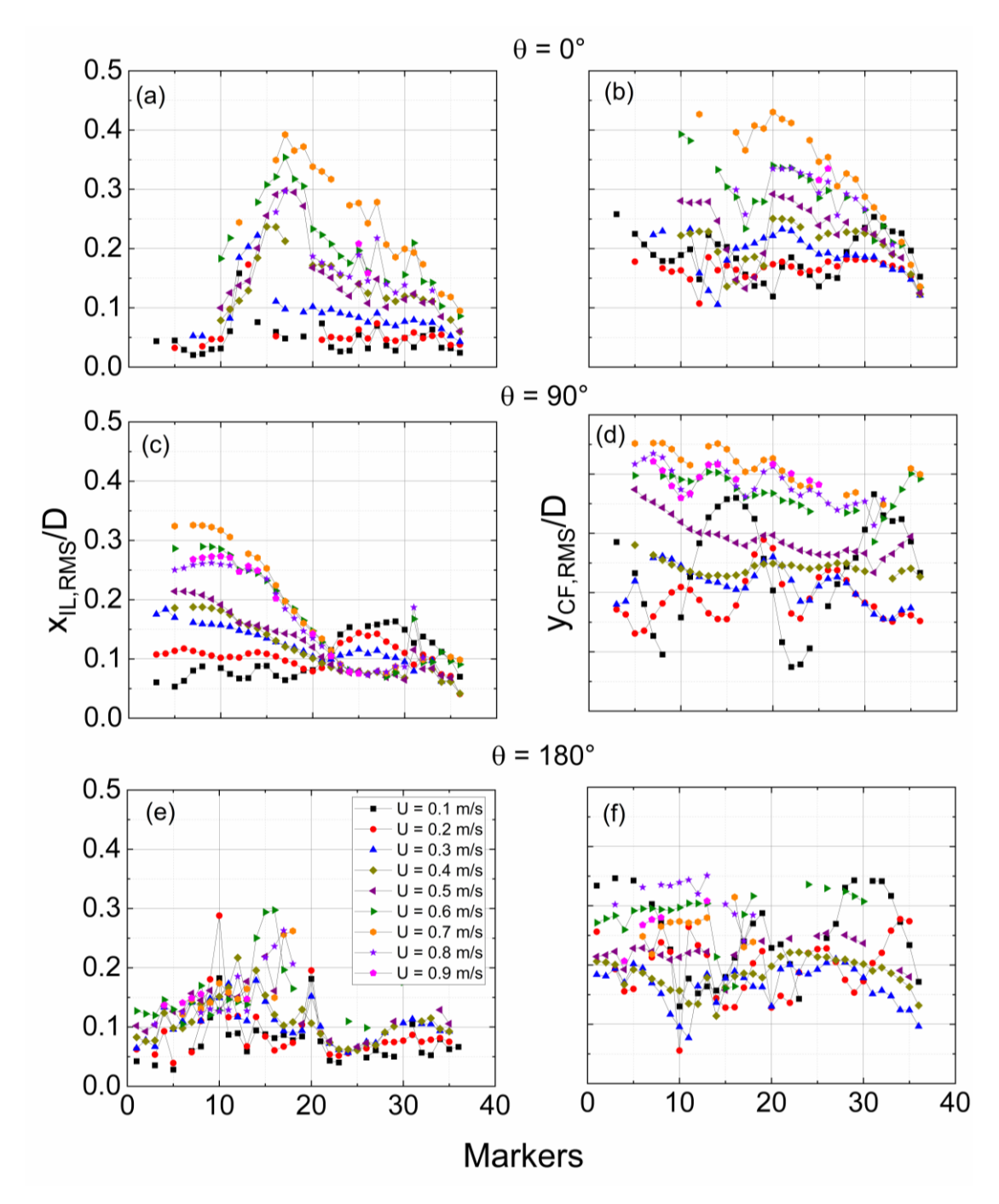


Figure 15: RMS normalised in-line and cross-flow displacements of all markers in currents of different speeds: (a) IL, θ = 0°; (b) CF, θ = 0°; (c) IL, θ = 90°; (d) CF, θ = 90°; (e) IL, θ = 180°; (f) CF, θ = 180°.

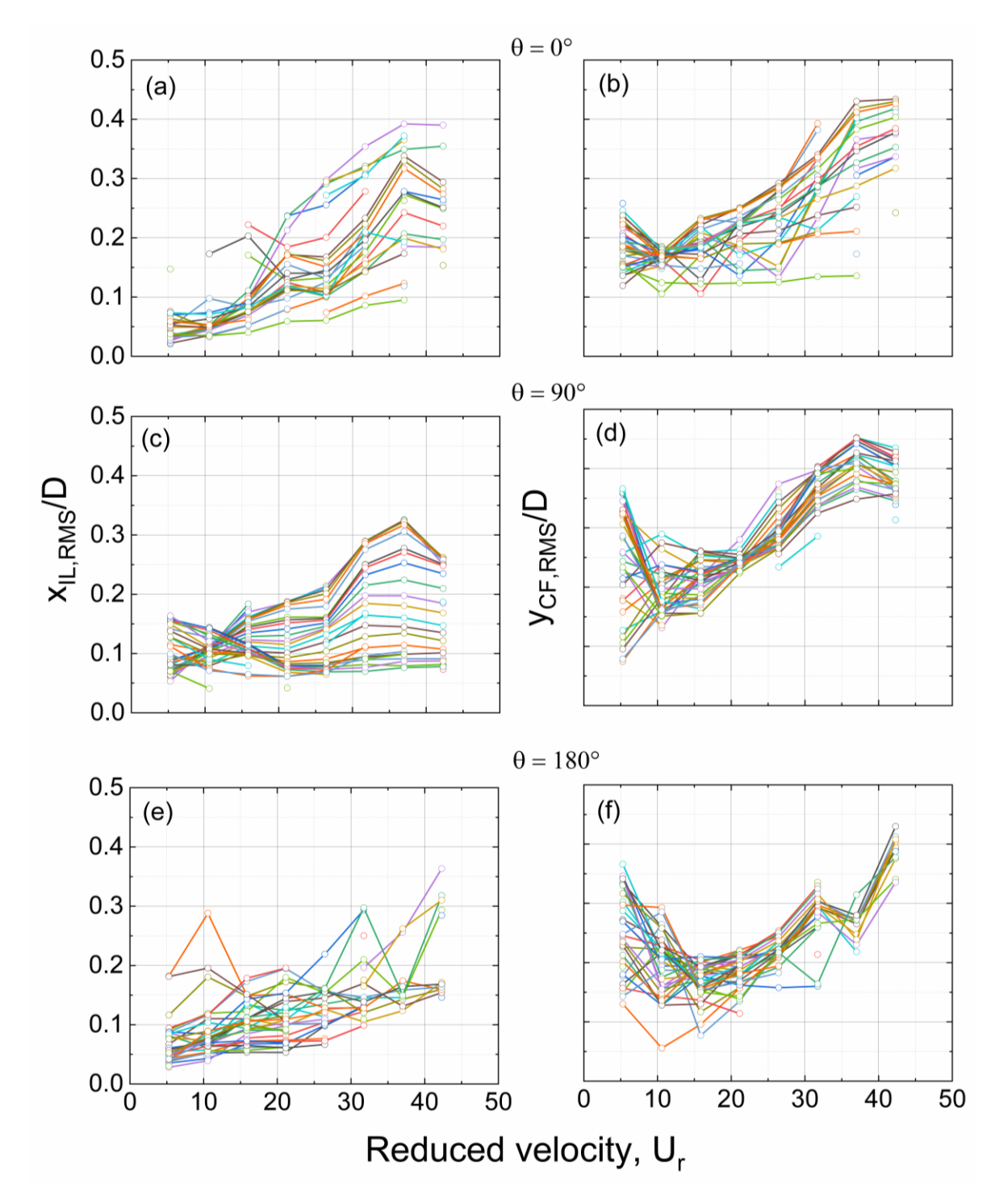


Figure 16: RMS normalised inline and crossflow displacements of all markers as functions of reduced velocity: (a) IL, θ = 0°; (b) CF, θ = 0°; (c) IL, θ = 90°; (d) CF, θ = 90°; (e) IL, θ = 180°; (f) CF, θ = 180°.

Figure 16 presents the root mean square normalised in-line ($x_{\rm IL,RMS}/D$) and cross-flow displacements ($y_{\rm CF,RMS}/D$) as functions of reduced velocity (U_r) for all marker locations along the cable. Unlike observations reported in the literature for short rigid cylinders, where synchronization zones or lock-in regimes are typically identified, the results obtained here do not exhibit such distinct regimes. While this trend may superficially resemble the "infinite lock-in" phenomenon described in the literature for critical mass

ratios (e.g. Govardhan & Williamson, 2002 and Horowitz & Williamson, 2010), it is important to note that the cable in this study has a high mass ratio and does not exhibit classical lock-in behaviour, which typically occurs at lower mass ratios (e.g., 0.542).

The main reason for this is the geometry of lazy wave cable which is free to move in all six degrees of freedom, unlike the more constrained configurations considered in previous studies. Variations in displacement exhibit stepwise increases and irregular reductions which may be attributed to synchronization occurring for U_r in the range 5 to 15, followed by transition to a second-order synchronization for $U_r \ge 20$. Unlike previous studies, we find no significant reduction in displacement at higher U_r . This contrasts with previous findings for cylinders of low mass ratio in uniform currents, which generally exhibit a broader lock-in range than their high mass ratio counterparts (as noted by Vandiver, 1993). Previous studies of uniform and sheared flows (Trim et al., 2005; Chaplin et al., 2005) have reported drastic displacement drops during mode switches and monotonically increasing displacement groups, neither of which were observed for our lazy wave model. Fluctuations in displacement levels along the length of the cable occurred at specific values of reduced velocity. Peak RMS values of the in-line and cross-flow displacement amplitudes ascribed to vortex-induced vibrations (VIV) observed herein are 0.39D (at M17) and 0.41D (at M12) for $\theta = 0^{\circ}$, 0.40D (at M35) and 0.45D (at M7) for θ = 90°, and 0.26D (at M18) and 0.35D (at M13) for θ = 180°. As would be expected, the maximum displacement varies along the lazy wave cable. For $\theta = 0^{\circ}$ (Figure 16 (a & b)), the RMS normalized in-line and cross-flow displacements remain relatively consistent along the cable length up to a reduced velocity of 15. Beyond this threshold, the RMS displacement magnitudes diverge significantly among the different markers. This behaviour can be correlated with the displacement plots in Figure 9, where higher current speeds induce more pronounced changes in the response of the cable. Thus, the flow is not incident normal along the cable length, causing differences in the hydrodynamic loading at each marker location. Additionally, the stiffness and tension of the cable vary along its length, which can further explain the observed divergence in displacement magnitudes. At certain locations, where the cable may be slack, the displacement tends to be larger due to reduced restoring forces. On the other hand, sections of the cable under higher tension are stiffer, and their displacement is more constrained. This combination of varying hydrodynamic forces, stiffness, and tension along the cable contributes to the observed differences in displacement response at higher velocities.

The cross-flow displacement shows a non-monotonic trend with reduced velocity, characterized by an initial increase, a drop, and then another increase, implying the onset of different vortex shedding modes and transitions between them. For θ = 90° (Figure 16 (c & d)), both in-line and cross-flow RMS displacements exhibit consistent variations across the markers as the reduced velocity increases. As with the θ = 0° results, the displacements generally increase with reduced velocity, though with more pronounced scatter, indicating a more complicated response when θ = 90°. For θ = 90° (Figure 16 (e)), the in-line displacement tends to increase with U_r , though with greater variability than for θ = 0° and 180°. This variability is most likely caused by the

reversed flow direction, leading to different force distributions and displacement variations along the cable. Conversely, for θ = 180° (Figure 16 (f)), the cross-flow displacement behaviour is narrower across the markers, indicating a more uniform structural response, particularly at higher U_r . For all current directions, the cross-flow displacements exhibit non-monotonic behaviour, suggesting complex interactions between the cable and the flow, possibly due to varying vortex shedding modes or resonant frequencies excited at different reduced velocities. The differences in displacement patterns obtained for $\theta = 0^{\circ}$, 90°, and 180° imply that the angle between the flow direction and cable axis has a significant influence, intensified by asymmetry in the structural properties of the cable. The scattered displacement data imply the excitation of different vibration modes along the cable length, which have a knock-on effect on the responses. The cable may be experiencing a combination of bending and torsional modes, which are contributing to its complex dynamic behaviour. These observations accord with findings from studies of long flexible cylinders with higher aspect ratios (Swithenbank et al., 2008) and of flow-induced oscillations of circular cylinders arranged in tandem (Assi et al., 2006). Our results highlight the effect of flow interference along the length of the lazy wave cable.

3.3 Cable Response Spectra

Spectral analysis was performed on the normalized in-line and cross-flow displacement time signals to identify the peak frequencies of vibration of the cable in different current directions. Figures 17, 18 and 19 display the in-line and cross-flow displacement spectra obtained for the cable in currents of direction $\theta = 0^{\circ}$, 90° , and 180° and speed U = 0.1, 0.3, 0.5 and 0.7 m/s. Each spectrum is plotted as a function of normalized frequency f/f_m , where f is the IL (f_{IL}) or CF (f_{CF}) frequency and f_m is the modal frequency obtained from OrcaFlex. The inline frequency is normalized by $f_{m(2)} = 0.127$ Hz in the X-plane and crossflow normalized by $f_{m(3)} = 0.1857$ Hz in the Y-plane. Each plot includes spectra from all available marker locations, with peak frequencies highlighted. The spectral peak frequencies obtained from the spectra, with all marker locations being indicated. Although some fluctuations in frequency occur, the peaks consistently repeat, as seen in the spectra.

Figure 20 further illustrates the relationship between the peak in-line and cross-flow frequency ratios, $f_{\text{IL,p}}/f_{m(2)}$ and $f_{\text{CF,p}}/f_{m(3)}$, and the reduced velocity U_r across the three current directions. The superimposed black dashed lines correspond to the natural frequencies ($f_{m(1)}$ to $f_{m(25)}$) computed using modal analysis for modes 1 to 25 as shown on Table 2 (for up to 15 modes). Frequency curves corresponding to Strouhal number ($St = f_{st}D/U$) values of 0.1, 0.15 and 0.2 are also superimposed to identify regions where VIV and/or modal response may be activated. The aim is to determine which frequencies are excited at each U_r value and how they match with the modal frequencies.

We first consider the displacement spectra obtained for the cable in the current directed at $\theta = 0^{\circ}$ (Figure 17). For a low current speed of U = 0.1 m/s, the cross-flow (CF) and inline (IL) displacement spectra exhibit multiple peaks. The primary energetic peak frequency in CF occurs at $f_{CF}/f_m = 3.03$, with secondary peaks at 2.19 and 1.35 (Figure 17b). Similarly, the IL spectrum shows dominant peaks at $f_{\parallel}/f_m = 1.92, 3.12$, and 4.33 (Figure 17a). The higher peak frequencies at $f/f_m \approx 3$ and 4 indicate the excitation of vibration modes that are approximately 3 to 4 times the structure's natural frequency. The consistency of peak locations across marker positions indicates that a fundamental vibration mode is dominant along the entire length of the cable. At U = 0.3 m/s, the highest peak at f_{IL}/f_m = 4.33 in the IL spectrum disappears, and the primary peak shifts to $f_{IL}/f_m = 1.68$ (Figure 17c), which corresponds to the 5th modal frequency in the inline direction (Table 3). In CF (Figure 17d), the primary peak shifts to $f_{CF}/f_m =$ 1.18, with a secondary peak at $f_{CF}/f_m = 3.53$, which is likely a VIV component. For U = 0.5 m/s, both the IL and CF spectra display multiple frequency peaks, indicating complex vibrational behaviour. The primary peak in IL occurs at $f_{\parallel L}/f_m = 1.92$, while CF exhibits a dominant peak at $f_{CF}/f_m = 1.35$, with additional peaks at 1.68, 2.52, 3.03, and 3.87 (Figure 17e & f). These frequencies suggest mode interactions and potential energy transfer between vibration modes. At U = 0.7 m/s (Figure 17g & h), the IL response remains dominated by $f_{IL}/f_m = 1.68$, while the CF response shows a strong peak at f_{CF}/f_m = 1.35, with smaller peaks at 2.86 and beyond.

Examining the frequency variation with reduced velocity (Figure 20 a & b), the first peak frequencies correspond to the 4th inline modal frequency and the 1st cross-flow modal frequency. Additionally, f_{IL}/f_m remains nearly constant across different current speeds, indicating strong modal influence and limited dependence on reduced velocity. However, the primary peak frequency ratio shifts towards $f_{CF}/f_m = 4.33$ and $f_{IL}/f_m = 3.03$ for Ur < 15, aligning with vortex-induced vibration (VIV) behaviour. At lower reduced velocities (Ur < 11), the higher Strouhal number ($St \approx 0.1$ –0.15) and the growth of the third spectral peak in CF displacement suggest enhanced vortex shedding contributions.

For $\theta = 90^\circ$ and U = 0.1 m/s (Figure 18 (a, b)), a sharp, dominant peak appears at $f/f_m \approx 3.61$ and 2.52 in both the in-line and cross-flow displacement spectra, indicating strong resonance at a single frequency across all markers. As the flow speed increases to U = 0.3 m/s (Figure 18 (c, d)), the spectra start to exhibit multiple peaks. In the in-line direction, the primary peak shifts to $f_{IL}/f_m \approx 1.92$, with additional peaks at $f_{IL}/f_m \approx 8.65$ and $f_{IL}/f_m \approx 10.82$, indicating the onset of more complex oscillatory behaviour. Similarly, the cross-flow displacement spectrum shows a dominant peak at $f_{CE}/f_m \approx 1.18$, along with secondary peaks, reflecting a broader frequency response. At U = 0.5 m/s (Figure 18 (e, f)), the spectral complexity increases further. The in-line displacement spectrum maintains a primary peak at $f_{IL}/f_m \approx 1.92$, but with significant secondary peaks at higher frequency ratios ($f_{IL}/f_m \approx 6.49$ to 16.35). In the cross-flow direction, the dominant peak occurs at a similar frequency ratio, but the energy distribution broadens, with notable peaks at $f_{CE}/f_m \approx 8.08$ to 13.13. For U = 0.7 m/s (Figure 18 (g, h)), the in-line and cross-flow displacement spectra continue to show

dominant peaks at $f/f_m \approx 1.92$ and 1.18 respectively, while additional peaks spread across a wide frequency range. Notable secondary peaks appear at $f_{CF}/f_m \approx 2.88$, 11.44, 13.94, and 17, suggesting that at higher velocities, flow-induced vibrations become more chaotic. The multiple peak frequencies in both displacement spectra (Figure 20b) arise because the entire length of the cable is perpendicular to the current direction. This is in contrast to $\theta = 0^\circ$, where the cable aligns longitudinally with the current, potentially causing slight blockage effects. Multiple peak frequencies appear for Ur = 15 to 21 in both the in-line and cross-flow response spectra. Figure 20b shows how the first four vibration modes of f_{IL}/f_m and f_{CF}/f_m increase with rising Ur, following trends in Strouhal numbers (St_x , $St_y \approx 0.1$ to 0.15). This provides evidence of prevalent vortex shedding with increasing reduced velocity. The CF frequencies are associated with a higher Strouhal number than the IL components. However, no components exceed a Strouhal number of 0.15 in these cases.

For $\theta = 180^{\circ}$ and U = 0.1 m/s, the in-line and cross-flow displacement spectra exhibit dominant peaks at $f_{IL}/f_m \approx 3.20$ and $f_{CF}/f_m \approx 2.19$, with small secondary peaks at some marker locations (Figure 19 (a, b)). As the current speed increases, multiple peaks emerge, particularly in the cross-flow displacement spectrum, indicating a more complex oscillatory response (Figure 19 (c, d, e, f)). By U = 0.7 m/s (Figure 19 (g, h)), the spectrum reveals a broad energy distribution across several frequencies, as flowinduced vibrations become increasingly chaotic. The relationship between reduced velocity and frequency ratio at $\theta = 180^{\circ}$ (Figure 20 (c)) differs from the $\theta = 0^{\circ}$ case, due to the angle of attack of the current with respect to the cable's longitudinal axis. At θ = 180°, the top portion of the cable is exposed first, and the bottom part is pushed backward later as the current speed increases. Multiple frequencies are present in the in-line and cross-flow responses up to Ur = 21 (Figure 20 (c)), but at higher Ur values, the response shifts to a lower frequency range. The peak normalized frequencies in the in-line direction for Ur < 21 correspond to St values between 0.12 and 0.14. Similarly, the peak frequencies in the cross-flow direction increase with Ur, aligning with St values around 0.10.

As the flow speed increases from 0.1 to 0.7 m/s, the spectral analysis reveals a shift in the dominant frequency and the emergence of multiple peaks, reflecting increased complexity in the system's dynamic response. At lower current speeds, the system exhibits a strong resonance near a single frequency, particularly in the cross-flow direction where the magnitude of the response is of higher magnitude. However, as the flow speed increases, the spectra become increasingly complex, with energy distributed across a broader range of frequencies in both the inline and cross-flow directions, indicating the propensity toward chaotic flow-induced vibrations. This transition is particularly evident in the cross-flow direction, where the spectral peaks become more pronounced and diverse, highlighting the sensitivity of the cross-flow response to changes in flow speed. High damping of the lazy wave cable in water could also contribute to the low VIV response. It should be noted that the lazy wave configuration can itself introduce additional damping. The slack sections and varying

curvature in the cable can absorb and dissipate more energy than a taut, straight cable.

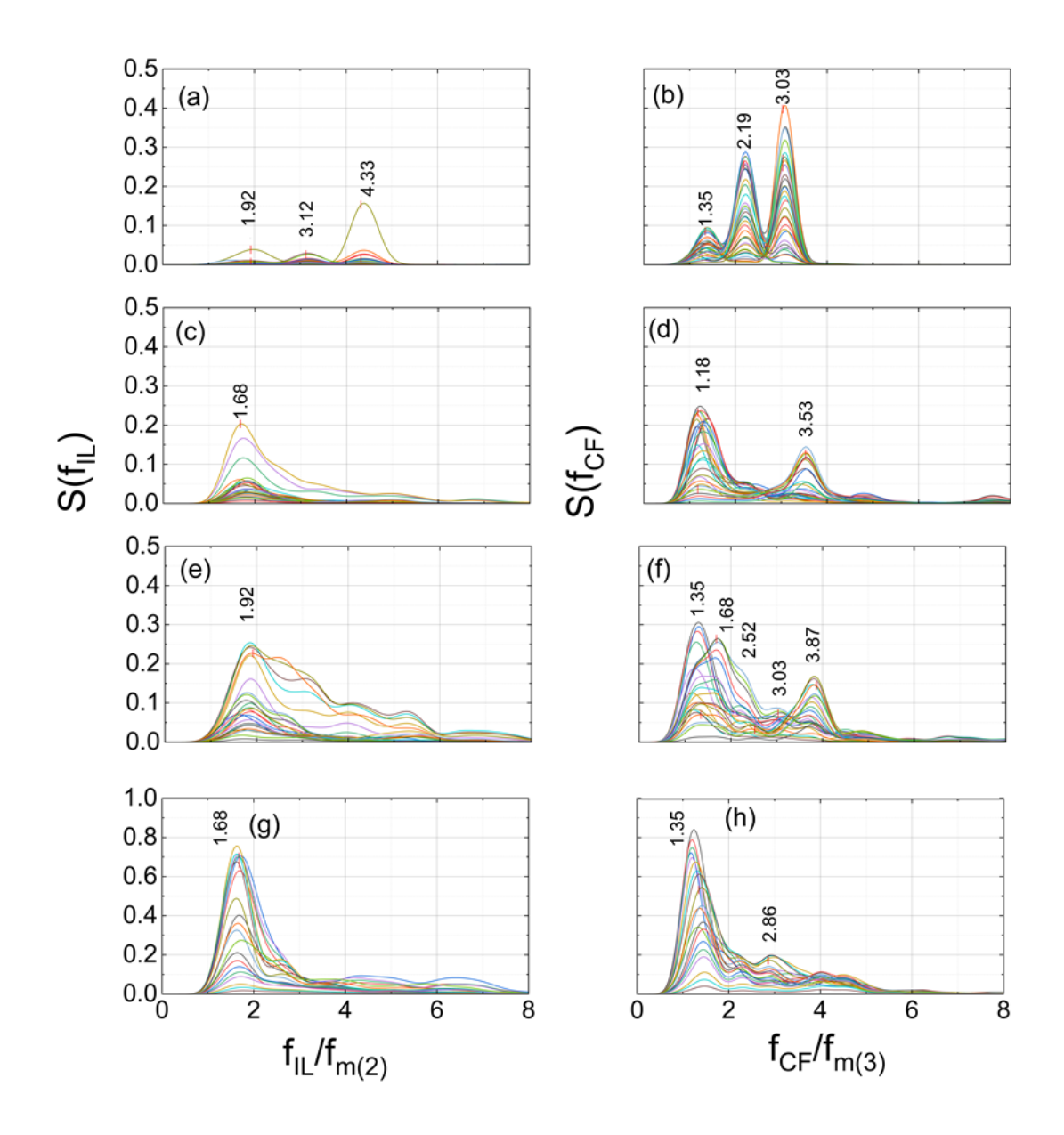


Figure 17: Measured in line and cross-flow displacement spectra at all marker locations for current at θ = 0°: (a) IL, U = 0.1 m/s; (b) CF, U = 0.1 m/s; (c) IL, U = 0.3 m/s; (d) CF, U = 0.3 m/s; (e) IL, U = 0.5 m/s; (f) CF, U = 0.5 m/s; (g) IL, U = 0.7 m/s; (h) CF, U = 0.7 m/s.

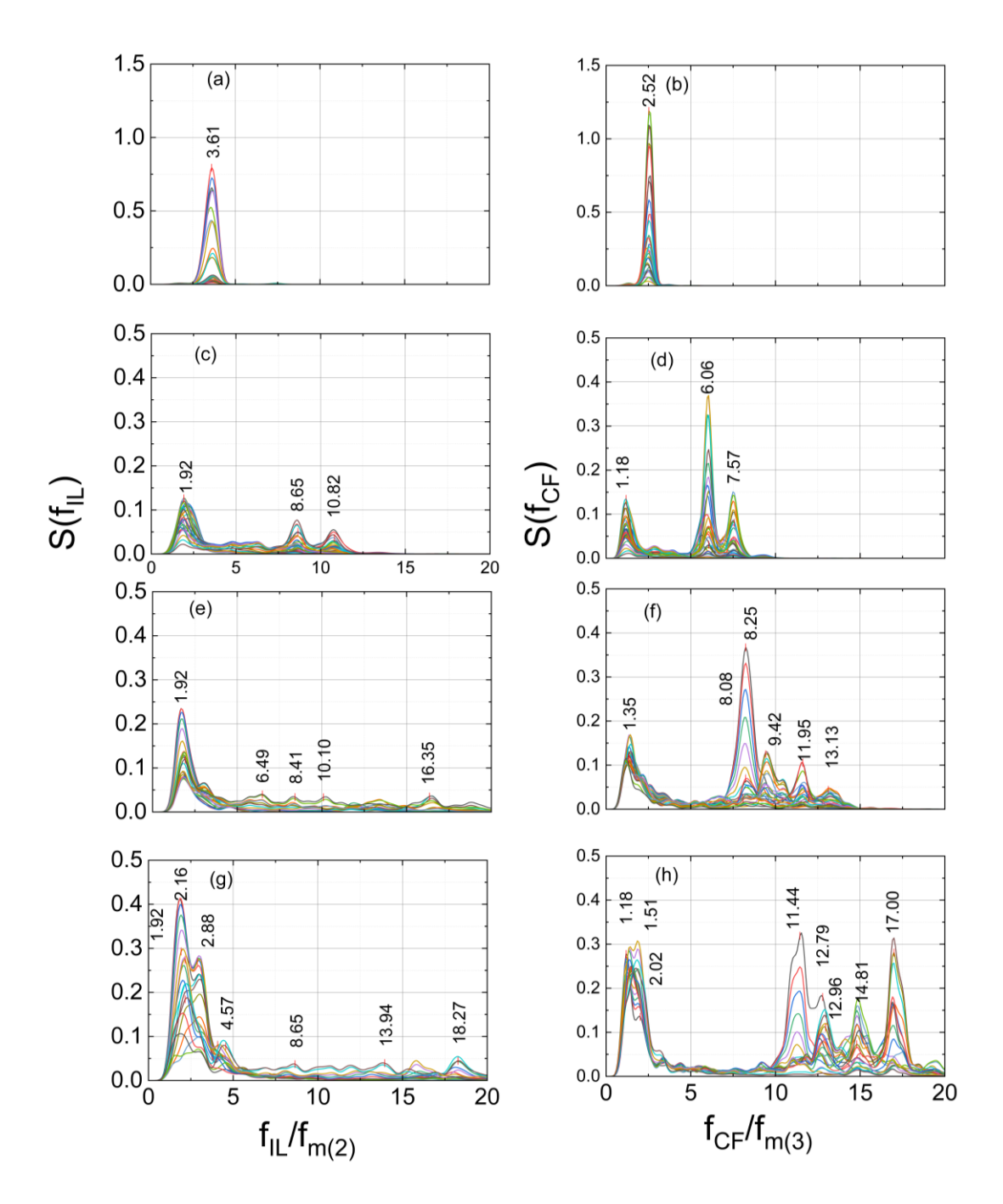


Figure 18: Measured in line and cross-flow displacement spectra at all marker locations for current at θ = 90°: (a) IL, U = 0.1 m/s; (b) CF, U = 0.1 m/s; (c) IL, U = 0.3 m/s; (d) CF, U = 0.3 m/s; (e) IL, U = 0.5 m/s; (f) CF, U = 0.5 m/s; (g) IL, U = 0.7 m/s; (h) CF, U = 0.7 m/s.

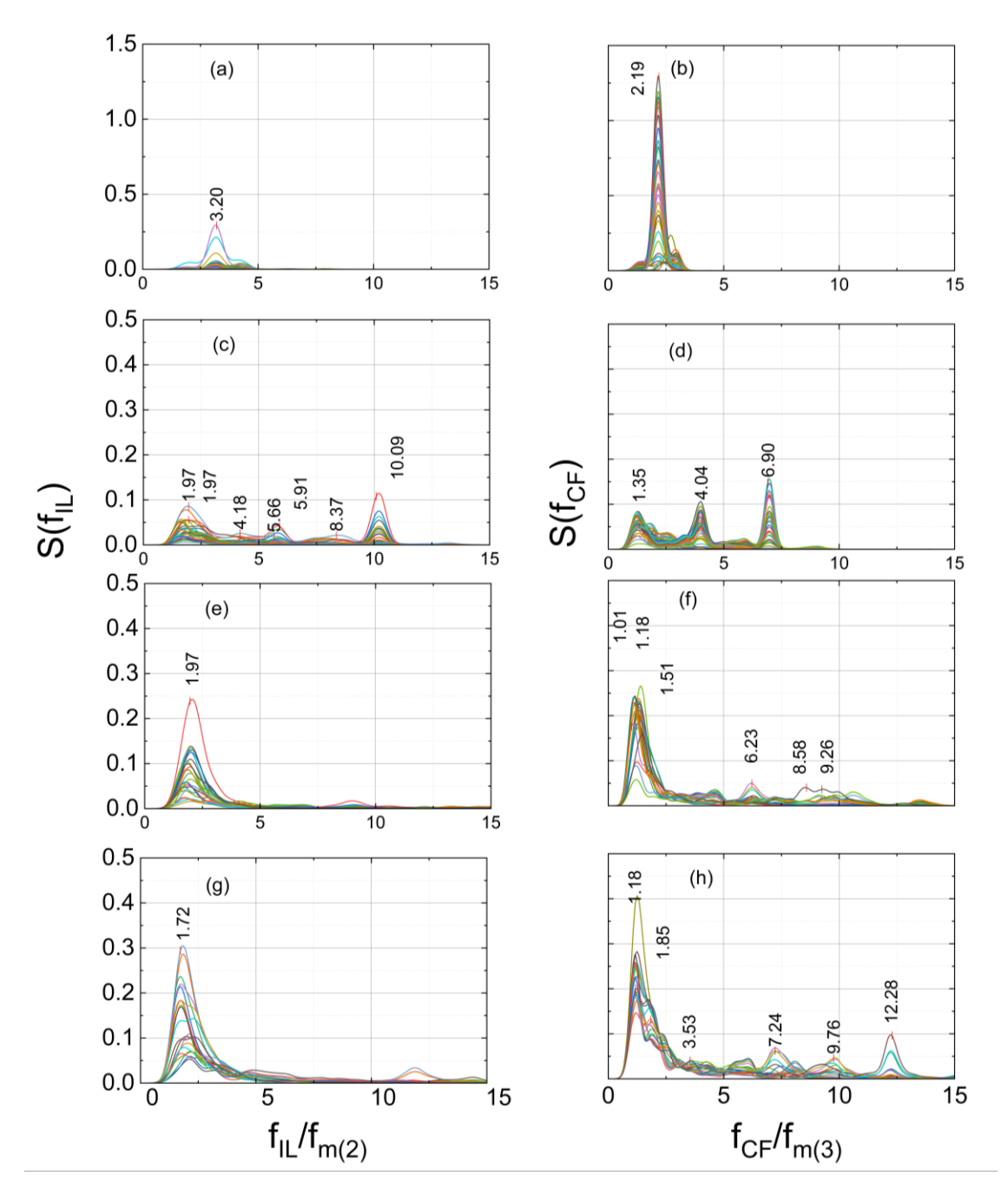


Figure 19: Measured in line and cross-flow displacement spectra at all marker locations for current at θ = 180°: (a) IL, U = 0.1 m/s; (b) CF, U = 0.1 m/s; (c) IL, U = 0.3 m/s; (d) CF, U = 0.3 m/s; (e) IL, U = 0.5 m/s; (f) CF, U = 0.5 m/s; (g) IL, U = 0.7 m/s; (h) CF, U = 0.7 m/s.

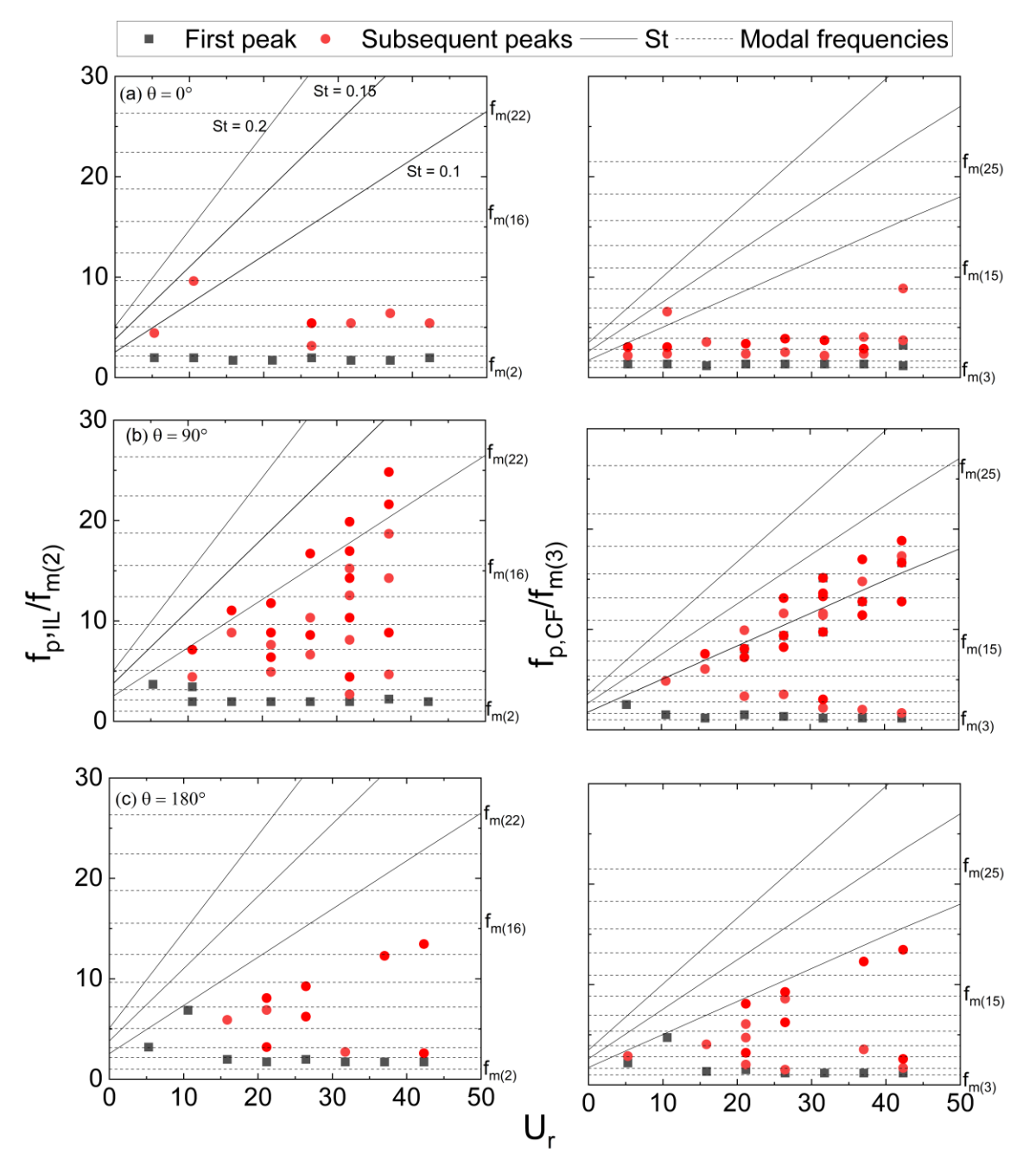


Figure 20: Dependence of in-line $(f_{IL}/f_{m(2)})$ and cross-flow $(f_{CF}/f_{m(3)})$ frequency ratios on reduced velocity (U_r) for current directions: (a) IL, $\theta = 0^\circ$; (b) CF, $\theta = 0^\circ$; (c) IL, $\theta = 90^\circ$; (d) CF, $\theta = 90^\circ$; (e) IL, $\theta = 180^\circ$; (f) CF, $\theta = 180^\circ$. Superimposed curves correspond to Strouhal numbers of 0.1, 0.15, and 0.2.

The results indicate that at lower reduced velocity, when the cable experiences minimal deflection, the response is dominated by higher value of peak frequency. As the current speed increases and the cable begins to deflect from its lazy wave shape, the response transitions from being dominated by pure vortex-induced vibration (VIV) to modal excitation, where the flow stimulates the cable's inherent structural modes. However, small-magnitude VIV contributions remain present, as highlighted in the Variational Mode Decomposition (VMD) analysis. Although alignment of peak frequency with the first natural frequency is evident, lock-in is not strictly evident.

Instead, the response exhibits a range of frequency components, leading to the cable undergoing a highly chaotic and non-stationary trajectory. This complexity makes it challenging to definitively conclude whether frequency lock-in has occurred or not. While lock-in might be present intermittently, the response lacks stationarity and repeatability, distinguishing it from more tensioned riser systems where VIV lock-in is more pronounced (Chaplin, 2005). This behaviour is characteristic of the lazy wave configuration, which facilitates greater flexibility and multi-modal interactions compared to taut or catenary risers. Increased structural compliance leads to a broader spectrum of excited frequencies rather than distinct, persistent lock-in events. Overall, these findings highlight the complex interplay between VIV and modal excitation in lazy wave configurations. Unlike tensioned risers, where VIV lock-in is more distinct, the flexible nature of the lazy wave system results in a dynamic response that varies across different flow conditions.

It is important to note that the reduced velocity values presented here are based on the global current velocity magnitude. In practice, the effective forcing on each cable segment depends on the local velocity component normal to the cable. As such, the method used to calculate velocity can influence the results. While projecting the velocity onto the local normal vector and iteratively computing normalized quantities would improve accuracy, such an approach demands significantly more detailed spatial resolution and computational effort. This refinement is acknowledged as a valuable direction for future work to improve the fidelity of VIV and modal interaction characterization in Lazy wave cable configurations.

4. Conclusions

The primary objective of this study was to examine the effects of flow-induced vibrations on a dynamic power cable model configured in a lazy wave arrangement at a laboratory scale. To achieve this, comprehensive laboratory measurements were conducted with currents of varying magnitudes and flow directions. The tests involved a meticulously chosen model cable with a diameter of 31 mm, characterized by low bending stiffness and a mass ratio of 1.22. The experimental investigation covered Reynolds numbers ranging from 10³ to 10⁴. Displacements at 36 locations along the cable length were measured by a motion-capturing camera and analysed in the paper. The results bring to light the intricate behaviour of the lazy wave power cable, offering valuable insights.

The maximum RMS displacements of the cable were found to be around 0.45 D for increasing current velocities across three current directions considered. Spectral analysis revealed a mono frequency response at lower reduced velocities and a multiple frequency response with distributed energy at higher reduced velocities. The peak frequencies normalized with the natural frequency in air showed an increasing pattern for current direction of 90° but decreased below $f_s/f_n < 1$ for current directions 0° and 90°. Frequency synchronization was evident in both in-line (IL) and cross-flow (CF) directions. The Time-frequency analysis indicated that the low-frequency peak

was not continuous over time but instantaneous, with higher frequencies corresponding to higher Strouhal numbers present throughout the time, confirming the presence of Vortex-Induced Vibrations (VIV).

Low frequency vibrations were observed at higher reduced velocities, though vortex shedding corresponding to a Strouhal number of 0.12 was also present. However, there was a lack of periodicity and no clear lock-in phenomenon was observed, with a higher likelihood of lock-in occurring at lower reduced velocities of 5-10. At higher Reynolds numbers, structural modal instability becomes the dominant cause of vortex-induced vibrations (VIV), rather than resonance caused by lock-in. Despite the absence of mechanisms to observe the shedding patterns directly, it was inferred that the shed vortices were influenced by the profile of the cable and the presence of buoyancy modules, which contributed to damping the frequency components. The findings provide a detailed characterization of the dynamic responses of lazy wave configurations under varying flow conditions, emphasizing the complex interplay between structural dynamics and fluid forces.

References

- Assi, G. R. S., Bearman, P. W., & Kitney, N. (2009). Low drag solutions for suppressing vortex-induced vibration of circular cylinders. *Journal of Fluids and Structures*, *25*(4), 666–675. https://doi.org/10.1016/j.jfluidstructs.2008.11.002
- Assi, G. R. S., Meneghini, J. R., Aranha, J. A. P., Bearman, P. W., & Casaprima, E. (2006). Experimental investigation of flow-induced vibration interference between two circular cylinders. *Journal of Fluids and Structures*, 22(6–7), 819–827. https://doi.org/10.1016/j.jfluidstructs.2006.04.013
- Assi, G. R. S., Srinil, N., Freire, C. M., & Korkischko, I. (2014). Experimental investigation of the flow-induced vibration of a curved cylinder in convex and concave configurations. *Journal of Fluids and Structures*, 44, 52–66. https://doi.org/10.1016/j.jfluidstructs.2013.10.011
- Chaplin, J. R., Bearman, P. W., Huera Huarte, F. J., & Pattenden, R. J. (2005). Laboratory measurements of vortex-induced vibrations of a vertical tension riser in a stepped current. *Journal of Fluids and Structures*, *21*(1 SPEC. ISS.), 3–24. https://doi.org/10.1016/j.jfluidstructs.2005.04.010
- Chaplin, J. R., & King, R. (2018). Laboratory measurements of the vortex-induced vibrations of an untensioned catenary riser with high curvature. *Journal of Fluids and Structures*, 79, 26–38. https://doi.org/10.1016/j.jfluidstructs.2018.01.008
- Cheng, J., Cao, P., Fu, S., & Constantinides, Y. (2016). EXPERIMENTAL AND NUMERICAL STUDY OF STEEL LAZY WAVE RISER RESPONSE IN EXTREME ENVIRONMENT. *Proceedings of the ASME 2016 35th International Conference on Ocean, Offshore and Arctic Engineering OMAE2016 June 9-24, Busan, South Korea*. http://asmedigitalcollection.asme.org/OMAE/proceedings-pdf/OMAE2016/49965/V005T04A055/2531336/v005t04a055-omae2016-54871.pdf
- Fan, Y. ting, Mao, H. ying, Guo, H. yan, Liu, Q. hai, & Li, X. min. (2015). Experimental investigation on vortex-induced vibration of steel catenary riser. *China Ocean Engineering*, *29*(5), 691–704. https://doi.org/10.1007/s13344-015-0049-4

- Franzini, G. R., Pesce, C. P., Gonçalves, R. T., Fujarra, A. L. C., & Mendes, P. (2016). EXPERIMENTAL INVESTIGATIONS ON VORTEX-INDUCED VIBRATIONS WITH A LONG FLEXIBLE CYLINDER. PART I: MODAL-AMPLITUDE ANALYSIS WITH A VERTICAL CONFIGURATION. 11th International Conference on Flow-Induced Vibration, Hagues.
- Govardhan, R. N., & Williamson, C. H. K. (2006). Defining the "modified Griffin plot" in vortex-induced vibration: Revealing the effect of Reynolds number using controlled damping. *Journal of Fluid Mechanics*, *561*, 147–180. https://doi.org/10.1017/S0022112006000310
- Govardhan, R., & Williamson, C. H. K. (2002). Resonance forever: Existence of a critical mass and an infinite regime of resonance in vortex-induced vibration. *Journal of Fluid Mechanics*, 473, 147–166. https://doi.org/10.1017/S0022112002002318
- Horowitz, M., & Williamson, C. H. K. (2010). Vortex-induced vibration of a rising and falling cylinder. *Journal of Fluid Mechanics*, *662*, 352–383. https://doi.org/10.1017/S0022112010003265
- Huera Huarte, F. J., Bearman, P. W., & Chaplin, J. R. (2006). On the force distribution along the axis of a flexible circular cylinder undergoing multi-mode vortex-induced vibrations. *Journal of Fluids and Structures*, 22(6–7), 897–903. https://doi.org/10.1016/j.jfluidstructs.2006.04.014
- Huera-Huarte, F. J., & Bearman, P. W. (2009). Wake structures and vortex-induced vibrations of a long flexible cylinder-Part 1: Dynamic response. *Journal of Fluids and Structures*, *25*(6), 969–990. https://doi.org/10.1016/j.jfluidstructs.2009.03.007
- Jain, A., & Modarres-Sadeghi, Y. (2013). Vortex-induced vibrations of a flexibly-mounted inclined cylinder. *Journal of Fluids and Structures*, 43, 28–40. https://doi.org/10.1016/j.jfluidstructs.2013.08.005
- Jara-Bravo, C., Engineering, S., Minguez, M., Marty, A., La Seyne sur Mer, O., & Thierry Rippol, F. (2024). LAZY WAVE CABLES AND RISERS VIV RESPONSE: ON THE IMPACT OF BUOYANCY MODULES ASPECT RATIOS AND ARRANGEMENT.
- Lie, H., & Kaasen, K. E. (2006). Modal analysis of measurements from a large-scale VIV model test of a riser in linearly sheared flow. *Journal of Fluids and Structures*, 22(4), 557–575. https://doi.org/10.1016/j.jfluidstructs.2006.01.002
- Martinelli, L., Lamberti, A., Ruol, P., Ricci, P., Kirrane, P., Fenton, C., & Johanning, L. (2010). Power Umbilical for Ocean Renewable Energy Systems-Feasibility and Dynamic Response Analysis. 3rd International Conference on Ocean Energy, 6th October, Bilbao. https://www.researchgate.net/publication/228814942
- Moideen, R., Venugopal, V., & Chaplin, J. (2024). Vortex Induced Vibrations of a Lazy Wave Dynamic Power Cable Under Various Currents and Propagation Directions: Analysis Of Strain.
 Proceedings of the ASME 2024 43rd International Conference on Ocean, Offshore and Arctic Engineering. Volume 7: Ocean Renewable Energy. Singapore, Singapore., 9–14.

 http://asmedigitalcollection.asme.org/OMAE/proceedings-pdf/OMAE2024/87851/V007T09A037/7361615/v007t09a037-omae2024-126678.pdf
- Moideen, R., Venugopal, V., Chaplin, J. R., & Borthwick, A. G. L. (2025). VIV-induced strain on a lazy wave dynamic marine power cable in a steady current. *Ocean Engineering*, *328*. https://doi.org/10.1016/j.oceaneng.2025.121081

- Morooka, C. K., & Tsukada, R. I. (2013). Experiments with a steel catenary riser model in a towing tank. *Applied Ocean Research*, 43, 244–255. https://doi.org/10.1016/j.apor.2013.10.010
- Pereira, F. R., Gonçalves, R. T., Pesce, C. P., Fujarra, A. L. C., Franzini, G. R., & Mendes, P. (2013). *A MODEL SCALE EXPERIMENTAL INVESTIGATION ON VORTEX-SELF INDUCED VIBRATIONS (VSIV) OF CATENARY RISERS*. http://asmedigitalcollection.asme.org/OMAE/proceedings-pdf/OMAE2013/55416/V007T08A029/4431779/v007t08a029-omae2013-10447.pdf
- Pesce, C. P., Franzini, G. R., C Fujarra, A. L., Gonçalves, R. T., Salles, R., Mendes Riser, P., & Engineering, F. (2017). FURTHER EXPERIMENTAL INVESTIGATIONS ON VORTEX SELF-INDUCED VIBRATIONS (VSIV) WITH A SMALL-SCALE CATENARY RISER MODEL. http://journals.asmedigitalcollection.asme.org/OMAE/proceedings-pdf/OMAE2017/57649/V002T08A016/2532750/v002t08a016-omae2017-62100.pdf
- Quéau, L. M., Kimiaei, M., & Randolph, M. F. (2013). Dimensionless groups governing response of steel catenary risers. *Ocean Engineering*, *74*, 247–259. https://doi.org/10.1016/j.oceaneng.2013.03.020
- Raghavan, K., & Bernitsas, M. M. (2011). Experimental investigation of Reynolds number effect on vortex induced vibration of rigid circular cylinder on elastic supports. *Ocean Engineering*, *38*(5–6), 719–731. https://doi.org/10.1016/j.oceaneng.2010.09.003
- Rateiro, F., Pesce, C. P., Gonçalves, R. T., Fujarra, A. L. C., Franzini, G. R., & Mendes, P. (2016). EXPERIMENTAL INVESTIGATIONS ON VORTEX-INDUCED VIBRATIONS WITH A LONG FLEXIBLE CYLINDER. PART III: MODAL-AMPLITUDE ANALYSIS WITH A CATENARY CONFIGURATION. 11th International Conference on Flow-Induced Vibration, Hagues.
- Rentschler, M. U. T., Adam, F., & Chainho, P. (2019). Design optimization of dynamic inter-array cable systems for floating offshore wind turbines. *Renewable and Sustainable Energy Reviews*, 111, 622–635. https://doi.org/10.1016/j.rser.2019.05.024
- Resvanis, T. L., Jhingran, V., Vandiver, J. K., & Liapis, S. (2012). REYNOLDS NUMBER EFFECTS ON THE VORTEX-INDUCED VIBRATION OF FLEXIBLE MARINE RISERS. *Proceedings of the ASME 2012 31st International Conference on Ocean, Offshore and Arctic Engineering OMAE2012 July 1-6, 2012, Rio de Janeiro, Brazil*.
- Sarpkaya, T. (2004). A critical review of the intrinsic nature of vortex-induced vibrations. *Journal of Fluids and Structures*, *19*(4), 389–447. https://doi.org/10.1016/j.jfluidstructs.2004.02.005
- Srinil, N., Wiercigroch, M., & O'Brien, P. (2009). Reduced-order modelling of vortex-induced vibration of catenary riser. *Ocean Engineering*, *36*(17–18), 1404–1414. https://doi.org/10.1016/j.oceaneng.2009.08.010
- Swithenbank, S. B., Vandiver, J. K., Larsen, C. M., & Lie, H. (2008). Reynolds number dependence of flexible cylinder viv response data. *Proceedings of the International Conference on Offshore Mechanics and Arctic Engineering OMAE*, *5*, 503–511. https://doi.org/10.1115/OMAE2008-57045
- Thies, P. R., Johanning, L., & Smith, G. H. (2012). Assessing mechanical loading regimes and fatigue life of marine power cables in marine energy applications. *Proceedings of the Institution of Mechanical Engineers, Part O: Journal of Risk and Reliability, 226*(1), 18–32. https://doi.org/10.1177/1748006X11413533

- Trim, A. D., Braaten, H., Lie, H., & Tognarelli, M. A. (2005). Experimental investigation of vortex-induced vibration of long marine risers. *Journal of Fluids and Structures*, *21*(3 SPEC. ISS.), 335–361. https://doi.org/10.1016/j.jfluidstructs.2005.07.014
- Vandiver, J. K. (1993). DIMENSIONLESS PARAMETERS IMPORTANT TO THE PREDICTION OF VORTEX-INDUCED VIBRATION OF LONG, FLEXIBLE CYLINDERS IN OCEAN CURRENTS. *Journal of Fluids and Structures*, *7*, 423–455.
- Vandiver, J. K., Jaiswal, V., & Jhingran, V. (2009). Insights on vortex-induced, traveling waves on long risers. *Journal of Fluids and Structures*, *25*(4), 641–653. https://doi.org/10.1016/j.jfluidstructs.2008.11.005
- Williamson, C. H. K., & Govardhan, R. (2004). Vortex-induced vibrations. *Annual Review of Fluid Mechanics*, *36*, 413–455. https://doi.org/10.1146/annurev.fluid.36.050802.122128
- Xu, W., Ma, Y., Ji, C., & Sun, C. (2018). Laboratory measurements of vortex-induced vibrations of a yawed flexible cylinder at different yaw angles. *Ocean Engineering*, 154, 27–42. https://doi.org/10.1016/j.oceaneng.2018.01.113
- Yin, D. (2022). Heave Motion Induced Vortex-Induced Vibrations of a Full-Scale Steel Lazy Wave Riser. *Journal of Offshore Mechanics and Arctic Engineering*, 144(4). https://doi.org/10.1115/1.4054265
- Zhao, S., Cheng, Y., Chen, P., Nie, Y., & Fan, K. (2021). A comparison of two dynamic power cable configurations for a floating offshore wind turbine in shallow water. *AIP Advances*, *11*(3). https://doi.org/10.1063/5.0039221
- Zhu, H. jun, & Lin, P. zhi. (2018). Numerical Simulation of the Vortex-Induced Vibration of A Curved Flexible Riser in Shear Flow. *China Ocean Engineering*, *32*(3), 301–311. https://doi.org/10.1007/s13344-018-0031-z
- Zhu, H., Liu, W., & Zhou, T. (2020). Direct numerical simulation of the wake adjustment and hydrodynamic characteristics of a circular cylinder symmetrically attached with fin-shaped strips. *Ocean Engineering*, 195. https://doi.org/10.1016/j.oceaneng.2019.106756

APPENDIX A: Computation of in-line (x_{IL}) and cross-flow (y_{CF}) displacements of the cable in a current

The Qualisys system provides displacements of target points on the cable, on a frame of reference (X, Y, Z) that is fixed in space. Calculations set out below transform such measurements into in-line (IL) and cross-flow (CF) displacements, with reference to the local mean incident velocity. Time-averaged displacements due to the current are first subtracted from the measured time series. Time-dependent in-line and cross-flow displacements are described by the trajectory of the cable axis where it intersects the plane perpendicular to the mean local orientation of the cable. Cross-flow displacements lie in this plane, and are measured in the direction at right angles both to the cable axis and to the projection of the current. In-line displacements, also traced out on the normal plane, are perpendicular to both the cylinder's axis and the cross-flow direction.

Direction cosines are used to identify the orientations of the various axes involved in this transformation. The direction cosines of a line in space joining the points (X_1, Y_1, Z_1) and (X_2, Y_2, Z_2) are

$$l = (X_2 - X_1)/d$$
, $m = (Y_2 - Y_1)/d$, $n = (Z_2 - Z_1)/d$ (A.1)

where

$$d = \sqrt{(X_2 - X_1)^2 + (Y_2 - Y_1)^2 + (Z_2 - Z_1)^2}.$$
 (A.2)

It follows that

$$l^2 + m^2 + n^2 = 1 , (A.3)$$

and the angle between two intersecting lines with direction cosines I_1 , m_1 , n_1 and I_2 , m_2 , n_2 is

$$\cos \emptyset = l_1 l_2 + m_1 m_2 + n_1 n_2 . \tag{A.4}$$

The direction cosines of the axis of the cable between two adjacent Qualisys target points are known from their time averaged coordinates (X, Y, Z) and are denoted by I_c , m_c , n_c . Those for the direction of current are denoted by I_v , m_v and 0 (since the current has no vertical component). The FloWave experiments are identified by the current direction (θ) which is defined in Figure 6 and thus $Iv = -cos\theta$, $m_v = sin\theta$. The direction cosines of the cross flow and in-line directions, denoted I_{CF} , m_{CF} , n_{CF} and I_{IL} , m_{IL} , respectively are initially unknown. They are found from the geometrical relationships imposed through applications of equations (A.3) and (A.4)

$$\begin{split} n_{CF} &= \frac{-l_{c}m_{v} + l_{v}m_{c}}{\sqrt{(m_{c}^{2} + n_{c}^{2})l_{v}^{2} - 2l_{c}l_{v}m_{c}m_{v} + m_{v}^{2}(l_{c}^{2} + n_{c}^{2})}} \ , \\ m_{CF} &= \frac{-m_{c}n_{CF}n_{c} + \sqrt{-l_{c}^{2}(n_{CF}^{2} - 1)l_{c}^{2} + (m_{c}^{2} + n_{c}^{2})n_{CF}^{2} - m_{c}^{2}}}{l_{c}^{2} + m_{c}^{2}} \ , \\ l_{CF} &= \frac{-m_{CF}m_{c} - n_{CF}n_{c}}{l_{c}} \ , \\ n_{IL} &= \frac{-l_{CF}m_{c} + l_{c}m_{CF}}{\sqrt{(m_{c}^{2} + n_{c}^{2})l_{CF}^{2} - 2l_{c}(m_{CF}m_{c} + n_{CF}n_{c})l_{CF} + (m_{CF}^{2} + n_{CF}^{2})l_{c}^{2} + (m_{CF}n_{c} - m_{c}n_{CF})^{2}}}{\sqrt{l_{CF}^{2} - 2l_{c}(m_{CF}m_{c} + n_{CF}n_{c})l_{CF} + (m_{CF}^{2} + n_{CF}^{2})l_{c}^{2} + (m_{CF}n_{c} - m_{c}n_{CF})^{2}}} \ , \end{split}$$

and

$$l_{IL} = \frac{-m_{CF}m_{IL} - n_{CF}n_{IL}}{l_{CF}} \quad . \tag{A.5}$$

Finally, displacements in (X, Y, Z) coordinates can be transformed into the cross-flow and in-line directions by

$$y_{CF} = l_{CF}X + m_{CF}Y + n_{CF}Z$$

$$x_{IL} = l_{IL}X + m_{IL}Y + n_{IL}Z$$
 (A.6)

where x_{IL} and y_{CF} represent displacements in the in-line and cross-flow directions respectively.